AFRL-AFOSR-JP-TR-2018-0043

Bioinspired Engineering Synthesis Technology (BEST) for Active Photonic (NBIT III)

Luke Lee
REGENTS OF THE UNIVERSITY OF CALIFORNIA
2150 SHATTUCK AVE RM 313
BERKELEY, CA 94704-5940

03/19/2019
Final Report

DISTRIBUTION A: Distribution approved for public release.

Air Force Research Laboratory
Air Force Office of Scientific Research
Asian Office of Aerospace Research and Development
Unit 45002, APO AP 96338-5002

REPORT DOCUMENTATION PAGE

Form Approved
OMB No. 0704-0188

1. REPORT DATE *(DD-MM-YYYY)* 19-03-2019	**2. REPORT TYPE** Final	**3. DATES COVERED** *(From - To)* 14 Aug 2013 to 13 Aug 2017

4. TITLE AND SUBTITLE
Bioinspired Engineering Synthesis Technology (BEST) for Active Photonic (NBIT III)

5a. CONTRACT NUMBER

5b. GRANT NUMBER
FA2386-13-1-4120

5c. PROGRAM ELEMENT NUMBER
61102F

6. AUTHOR(S)
Luke Lee

5d. PROJECT NUMBER

5e. TASK NUMBER

5f. WORK UNIT NUMBER

7. PERFORMING ORGANIZATION NAME(S) AND ADDRESS(ES)
REGENTS OF THE UNIVERSITY OF CALIFORNIA
2150 SHATTUCK AVE RM 313
BERKELEY, CA 94704-5940 US

8. PERFORMING ORGANIZATION REPORT NUMBER

9. SPONSORING/MONITORING AGENCY NAME(S) AND ADDRESS(ES)
AOARD
UNIT 45002
APO AP 96338-5002

10. SPONSOR/MONITOR'S ACRONYM(S)
AFRL/AFOSR IOA

11. SPONSOR/MONITOR'S REPORT NUMBER(S)
AFRL-AFOSR-JP-TR-2018-0043

12. DISTRIBUTION/AVAILABILITY STATEMENT
A DISTRIBUTION UNLIMITED: PB Public Release

13. SUPPLEMENTARY NOTES

14. ABSTRACT

Nanoplasmonic science have attracted significant interest in various applications including electronics, photonics, energy, environmental and biomedical applications. However, their practical applications still require overcoming a few critical problems: (1) the rational design and scalable synthesis of unconventional nanostructures with superior properties, (2) active controls and orientation of nanostructures, and (3) efficient integration of nanostructures into functional devices. In order to challenge these problems, our team has focused on bioinspirations from nature where many complex structures are spontaneously produced by precise controls over chemical and physical processes on various interfaces. The objective of our collaborative research is to develop bioinspired engineering synthesis technology (BEST) by uncovering hidden treasures in the nature of various interfaces. In order to accomplish this objective, Sogang University has performed the synthesis and optimization of unconventional plasmonic nanoantennae and the active control of their motion. On the other hand, University of California at Berkeley has conducted the systematic characterization and optimization with multi-scale simulation, and the integration of plasmonic nanoantennae into microfluidic-based active devices for the biomedical applications.

15. SUBJECT TERMS
NBIT, Nanoscience, AOARD

16. SECURITY CLASSIFICATION OF:			**17. LIMITATION OF ABSTRACT**	**18. NUMBER OF PAGES**	**19a. NAME OF RESPONSIBLE PERSON**
a. REPORT	**b. ABSTRACT**	**c. THIS PAGE**			KNOPP, JEREMY
Unclassified	Unclassified	Unclassified	SAR		**19b. TELEPHONE NUMBER** *(Include area code)* 315-227-7006

Standard Form 298 (Rev. 8/98)
Prescribed by ANSI Std. Z39.18

Grant Number: FA2386-13-1-4120

Bioinspired Engineering Synthesis Technology (BEST) for Active Photonic (NBIT III)
(*Subtitle*: Bioinspired Interfacial Nanosystems for the Rational Synthesis, Active Control, and Application of Unconventional Plasmonic Nanoantennae)

Date: 13 November 2017

Name of Principal Investigators (PI and Co-PIs): Taewook Kang (Korea Team)

- e-mail address: twkang@sogang.ac.kr
- Institution: Sogang University
- Mailing Address: 35 Baekbeom-ro, Mapo-gu, Seoul 121-742, Korea
- Phone: +82-2-705-8920
- Fax: +82-2-705-8920

Name of Principal Investigators (PI and Co-PIs): Luke P. Lee (U.S. Team)

- e-mail address: lplee@berkeley.edu
- Institution: University of California, Berkeley (Departments of Bioengineering, EECS, and Biophysics Graduate Program)
- Mailing Address: #408C Stanley Hall, UC Berkeley, Berkeley, CA 94720, USA
- Phone: +1-510-642-5855
- Fax: +1-510-642-5835

Period of Performance: 08/14/2013 – 08/13/2017

**Note: NBIT is a collaborative research program with Korean scientists. Therefore, please include in the report your Korean partner's NBIT research results. Please clearly identify the research that was conducted by the Korean team and U.S. team.*

Abstract

Nanoplasmonic science have attracted significant interest in various applications including electronics, photonics, energy, environmental and biomedical applications. However, their practical applications still require overcoming a few critical problems: (1) the rational design and scalable synthesis of unconventional nanostructures with superior properties, (2) active controls and orientation of nanostructures, and (3) efficient integration of nanostructures into functional devices. In order to challenge these problems, our team has focused on bioinspirations from nature where many complex structures are spontaneously produced by precise controls over chemical and physical processes on various interfaces. The objective of our collaborative research is to develop bioinspired engineering synthesis technology (BEST) by uncovering hidden treasures in the nature of various interfaces. In order to accomplish this objective, Sogang University has performed the synthesis and optimization of unconventional plasmonic nanoantennae and the active control of their motion. On the other hand, University of California at Berkeley has conducted the systematic characterization and optimization with multi-scale simulation, and the integration of plasmonic nanoantennae into microfluidic-based active devices for the biomedical applications. Through closer collaboration between Sogang and Berkeley, some of our works were published in the high impact journals (*Advanced Materials* 2015, *Science Advances* 2016, *ACS Nano* 2016/2017, *Nano Letters* 2017 and *etc.*). Our bioinspired engineering synthesis technology (BEST) can generate effective solutions for innovative manufacturing of complex nanostructures. In addition, our method is environmentally benign, biocompatible, and green manufacturing process. Therefore, we strongly believe that our findings can greatly expand the utility of plasmonic nanoparticle in many applications.

I. Introduction

Plasmonic nanoparticles have a wide range of applications that involve molecular sensing, imaging, delivery, trapping, and manipulation owing to their biocompatibility, photostability, controllable photo-thermal property as well as high field enhancement. However, their practical applications are still limited to few conventional structures (e.g., sphere, rod, and thin film) due to the difficulty in (1) rational fabrication of unconventional plasmonic nanostructures with high field enhancement, tunable far-field resonance, and large surface area, (2) poor signal reproducibility associated with limited sensitivity and selectivity, and (3) sophisticated optical instruments. In order to challenge these limitations, we have focused on the natural phenomena giving many inspirations to us. For example, bioinspired interfacial reaction processes (i.e. biomineralization) in nature have drawn increased attention due to the ability to form marvelous materials with hierarchical structures and complex patterns associated with superior materials' properties. Likewise, we envision that the diversity of structures and patterns (e.g., corals, shells, diatoms, and snowflakes) generated from the natural phenomena could allow to rationally design new advanced plasmonic nanostructures.

The objective of this research is to develop bioinspired engineering synthesis technology (BEST) for uncovering hidden treasures in the nature of liquid-liquid or a liquid/superstructure interface via the rational synthesis of unconventional plasmonic nanostructures with superior optical property and high surface area, active control of nanoparticles' motion and orientation, and ultrasensitive and selective detection of trace molecules. For this purpose, we synthesized the unconventional plasmonic nanoantennae with a large surface area and numerous hot spots per each particle at a variety of interfaces including 'liquid/liquid interface', 'polymer/water interface', and 'liquid/virus interface' by carefully controlling the interfacial reactions and understanding interfacial reaction mechanisms with the aid of multi-scale simulation. More specifically, this research includes (1) the synthesis of the unconventional metallic nanoparticles with high surface area and superior optical properties at an liquid/liquid interface or an liquid/superstructure interface, (2) the optimization of physical and optical properties of the unconventional metal nanoparticles through multi-scale simulation, (3) the active control of the position and orientation of metallic nanoparticles at the interface by using multi-scale simulation, and (4) development of high-performance (i.e., sensitivity and selectivity) active plasmonic sensor platforms. The content of this research is as below:

- Synthesis of unconventional metallic nanostructures via precise control over the chemical reaction at a liquid/liquid interface or a liquid/superstructure interface
- Optimization of unconventional metallic nanostructures for strong near-field enhancement and tunable far-field response.
- Active control over the position and orientation of metallic nanostructures at a liquid/liquid interface or a liquid/superstructure interface by controlling interfacial energy.
- Large-area assembly of metallic nanostructures at a liquid/liquid interface or a liquid/superstructure.
- Rational design of unconventional metallic nanostructures via multi-scale simulations.
- Development of high performance (i.e., sensitivity and selectivity) active plasmonic sensor platform for molecule detection (biosensor and environmental monitoring)
- Development of interfacial nanosystems that can both synthesize metallic nanostructure and detect molecules

Above all, this research focus on (1) the design and synthesis of unconventional metallic nanostructures with high reproducibility, (2) active control over the position and orientation of metallic nanostructures at the interface, and (3) standardization of molecule detection technique. Our bioinspired engineering synthesis technology (BEST) can generate effective solutions for a new route to the formation of functional plasmonic materials as well as the development of new types of platforms for molecular detection of biologically and environmentally important analytes and soft-matter characterization.

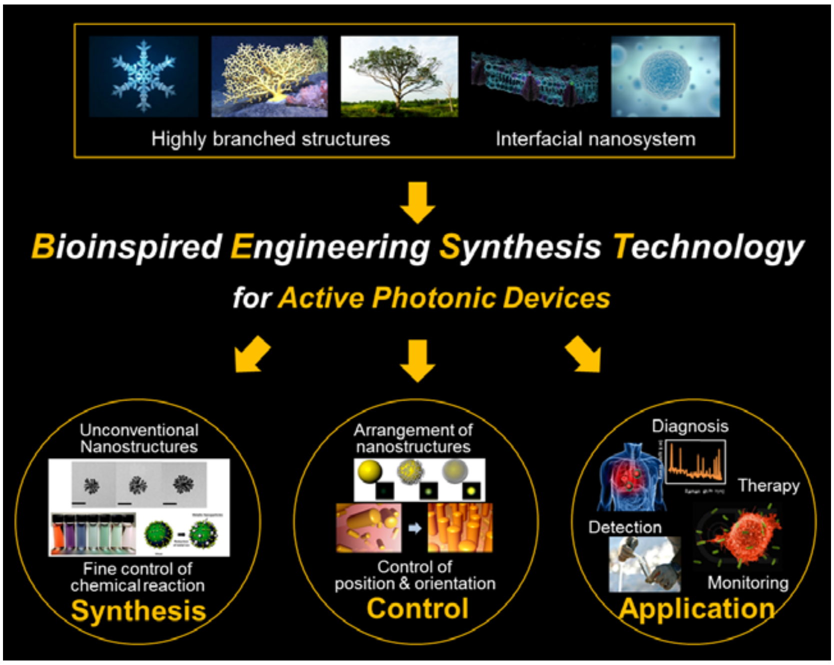

Figure 1. Schematic illustration of bioinspired engineering synthesis technology (BEST)

II. Research Scope and Accomplishment Methods by Year

Year	Research Scope	Accomplishment method	Contents
1st year	Bioinspired synthesis and characterization for unconventional nanoplasmonic thin films	Bioinspired synthesis of sub-100 nm plasmonic nanoantennae (e.g. snowflakes and plasmonic viruses)	- Synthesis and characterization of sub-100 nm plasmonic nanoantennae - Achievement of the increased surface area (> 120 %) compared to spherical nanoparticles - Achievement of strong electromagnetic field enhancement (> 10^9)
		Rational design and optimization of unconventional plasmonic nanoantennae	- Prediction of morphological characteristics of plasmonic nanoantennae via 3D multi-physics, -components, and –scales simulations - Optical simulation of plasmonic nanoantennae
2nd year	Active control of position and orientation of plasmonic nanoantennae in a thin film	Rational design and optimization of unconventional plasmonic nanoantennae	- Achievement of the increased surface area (> 130 %) compared to spherical nanoparticles - Achievement of electromagnetic field enhancement (> 10^{10}) compared to spherical nanoparticles
		Active control of position and orientation of plasmonic nanoantennae in a thin film	- Prediction of nanoparticle's position and orientation via simulation - Achievement of optical efficiency (> 200 %) compared to random position or orientation cases - Large-scale assembly (> 1mm ×1mm) of plasmonic nanoantennae
3rd year	Development of high performance active photonic sensor platforms	Performance improvement of the interfacial surface enhanced Raman scattering (SERS) technique	- Achievement of molecular level detection sensitivity for environmentally and biologically important target molecules (e.g., biomarker, environmental pollutants, and pathogens)
4th year	Ultrafast and Precise Identification of Waterborne Pathogens by Two-dimensional Nanoplasmonic Optical Antennas	Synthesis and optimization of nanoplasmonic optical antennas and their assemblies	- Controlling the aspect ratio, composition, surface chemical property and surface charge of metallic nanoparticles - Optimization of self-assembling metallic nanoparticles on the surface of pathogens via multi-scale simulation
		Development of integrated nanopore SERS for the detection of waterborne pathogens	- Integration of nanopore membrane to microfluidic system - Achievement of ultrafast (<10 min) and precise (10^2 cells/mL) identification of waterborne pathogens (*i.e.*, *Escherichia coli*, *Pseudomonas aeruginosa*)

III. Results

III-A. Results of 1st year

III-A-1. Synthesis of two-dimensional hyper-branched gold nanoparticles on a two-dimensional oil/water interface (Korea team)

Due to the unique properties, hyper-branched plasmonic nanoparticles have received much attention in the wide range of plasmonic applications. The unique structural features of these nanoparticles such as many branches and nanometer-sized gaps on a single particle allow high surface area-to-volume ratio for large loading capacity of molecules (e.g., drugs and genes) as well as tremendous hot-spots that can hugely enhance electromagnetic fields, enabling efficient therapy and precise diagnosis at the molecular level. Here, we synthesized such hyper-branched, sub-100 nm plasmonic gold snowflakes by utilizing bioinspired liquid/liquid interfaces. A gold precursor ($HAuCl_4 \cdot 3H_2O$) was dissolved in deionized water, followed by the addition of a reducing agent ($NH_2OH \cdot HCl$) into the aqueous solution. Oleic acid was then slowly poured on top of the solution. Approximately 4 min after the addition of the oleic acid, the liquid/liquid interface appeared light grey in color and gradually changed to pink. On the other hand, both water and oil layers remained colorless for over 30 min, indicating that the formation of the nanoparticles selectively takes place at the interface.

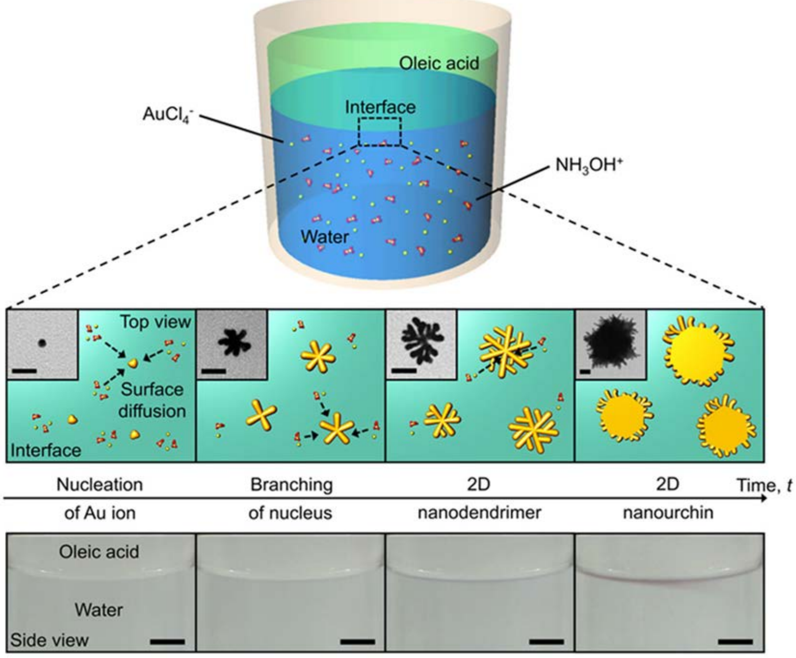

Figure 2. Schematic representation and time-resolved optical images of an oleic acid/water interface for the synthesis of two-dimensional gold nanoparticles

***Morphological and optical characterizations of 2D hyper-branched gold nanoparticles*:** In order to characterize the gold nanoparticles formed on the interface in detail, the oleic acid/water interface was sampled for transmission electron microscope (TEM) and atomic force microscope (AFM) measurements. To statistically analyze their morphological and structural transitions, 80 particles from each microscope image were randomly selected. Figure 3a shows representative TEM and AFM images of the gold nanoparticles collected from the interface at the early stage of growth (at 4 min after the addition of oleic acid). Clearly, the gold nanoparticles show a dendritic morphology along with primary and secondary branches (Figure 3a). The TEM images show that small gaps in the range of 2–8 nm exist between branches. Average lengths with respect to x, y, and z axes of the particles were 53.5 ± 10.4 nm, 54.2 ± 11.7 nm, and 4.21 ± 1.70 nm, respectively (Figure 3b and 3g), indicating that the gold nanoparticles are two-dimensional. As the reaction time proceeds, the small gaps between the branches are quickly filled with gold atoms and new branches are formed simultaneously. After 5 min, the morphology of the particles changed from nanodendrimer to nanourchin with many smaller branches (4–7 nm) on the outer surface (Figure 3e). The lengths of the nanourchin, with respect to x, y, and z axes were found to be 122.0 ± 26.5 nm, 123.0 ± 25.7 nm, and 5.03 ± 1.65 nm, respectively (Figure 3f and 3g). During this morphological transition, lateral sizes with respect to x and y axes increased by about 140% while the thickness (i.e., along z axis) remained nearly constant. This suggests that the gold nanoparticles formed on the oleic acid/water interface are likely to grow along the interface, maintaining their two-dimensional structure. As shown in Figure 3i, the final colloidal solution is dark grey in color. The absorbance spectrum of the solution exhibits two distinct surface plasmon resonance (SPR) bands at 525 and 828 nm. Two SPR bands in the visible and near-IR range can be attributed to the shape anisotropy of the particles.

III-A-2. Synthesis of plasmonic eu-viruses for optical nanoantennae for quantum nanobiology (U.S. team)

Owing to the unique morphologies and surface properties (i.e., evenly distributed chemical moieties), viruses can be excellent templates for the design and synthesis of novel nanomaterials/nanoarchitectures. The unique and detailed structures of viral capsids can be used as strong plasmonic templates by conjugating novel metals onto their surfaces. The plasmonic metal layer formed in this manner will function as an optical antenna to amplify and convert incident light into confined nanoscale volumes.

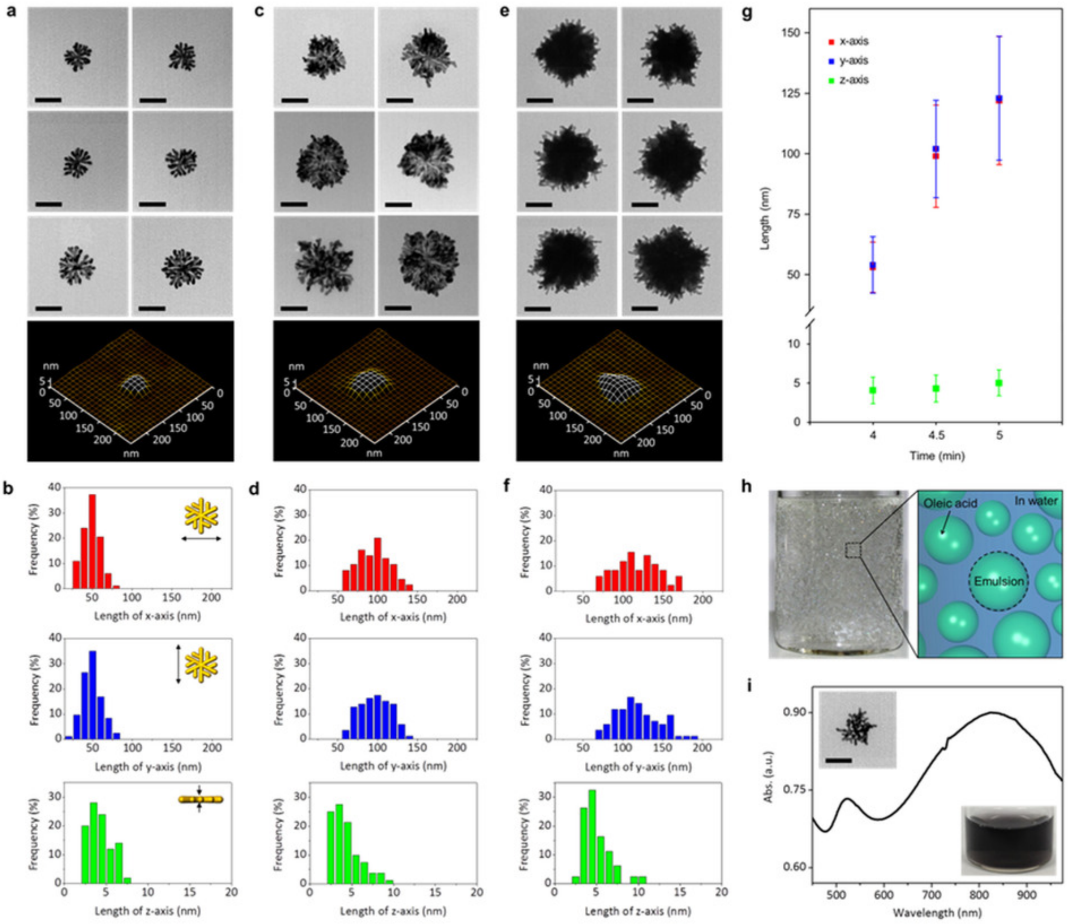

Figure 3 (a), (c), (e), Representative TEM and atomic force microscopy (AFM) images of 2D gold nanoparticles sampled at the interface at (a) 4 min, (c) 4 min 30 s, and (e) 5 min, respectively. (b), (d), (f), Size distributions with respect to x- (red), y- (blue) and z-axes (green) of the particles. (g), Average lengths with respect to x- (red), y- (blue) and z-axis (green) of the particles with increasing reaction time. (h), Optical image and corresponding cartoon of the interfacial synthesis via the oleic acid-in-water emulsion. (i), Representative UV-vis spectrum of the gold nanodendrimer synthesized at the oleic acid-in-water emulsion (top inset: TEM image of the nanoparticle, bottom inset: optical image of the solution). Scale bar is 50 nm.

Electromagnetic simulations of plasmonic eu-virus: The development of mathematical models of virus capsids could also enhance the potential for the application of viruses in molecular spectroscopic imaging. As an important aspect of viral studies, mathematical models have been developed to gain a fundamental understanding of viral structural and morphological analyses, classifications, and applications. These models can facilitate electromagnetic-field calculations of the optical response of a virus-template antenna. Using a topological description of an intriguing capsid model, we characterized the optical properties of our plasmonic eu-viruses compared to smooth plasmonic nanosphere. The simulation analysis explicitly indicated that the protrusions and valleys of capsid topology lead to the generation of more hot spots near the few-nanometer-distant tips of the gold structures than are created by the smooth surface of a nanosphere, which forms a single dome structure with a single edge (Figure 4).

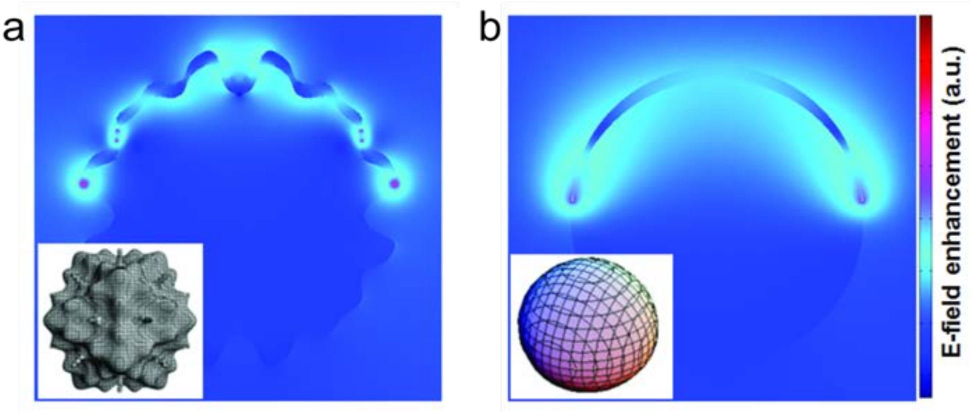

Figure 4 Electromagnetic simulations of (a) a plasmonic eu-virus and (b) a plasmonic nanosphere. The representative viral capsid structure was modeled using a mathematical expression. Both nanoparticles were scaled to 30 nm in diameter.

The electromagnetic energy comparison between the two types of structures clearly illustrates the advantages of the virus template. A plasmonic eu-virus generates more radiative energy and less resistive thermal energy in the gold layer (Figure 5). Thus, plasmonic eu-viruses can be useful in applications that utilize enhanced optical fields, such as sensitive and selective molecular imaging (i.e., vibration and absorption spectroscopy). Moreover, the lower resistive thermal energy may also be beneficial to the structural stability of the plasmonic eu-viruses under light excitation.

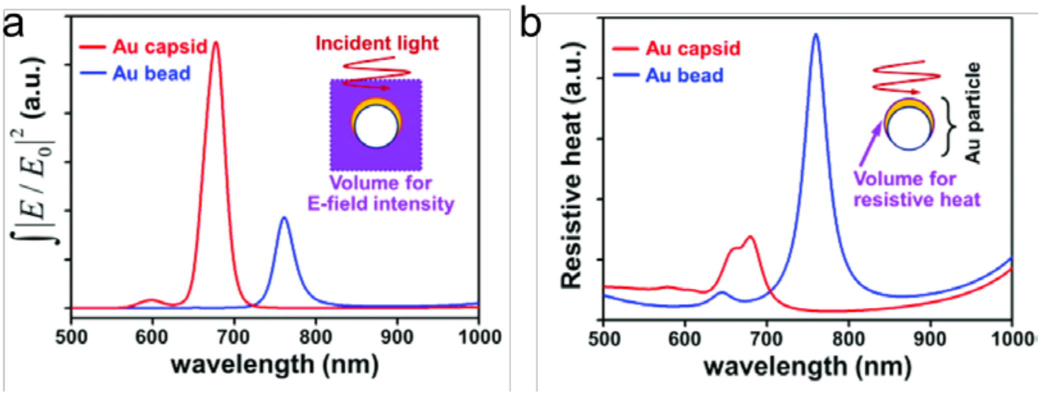

Figure 5. A comparison electromagnetic simulation of the (a) radiative and (b) resistive energies of the plasmonic eu-virus and plasmonic nanosphere. Simulation indicates that the plasmonic eu-virus enables molecular detection with improved sensitivity and stability.

Optical properties of various plasmonic eu-viruses: As a proof of concept, four types of well-characterized icosahedral plant viruses including belladonna mottle virus (BdMV), brome mosaic virus (BMV), tomato bushy stunt virus (TBSV), and cowpea mosaic virus (CPMV) were purified from infected plants, and thin gold layers of various thicknesses (1-10 nm) were coated onto the viruses via directional electron evaporation. Thereafter, the optical properties of these four different plasmonic eu-viruses were characterized by measuring their optical dark-field scattering signals (Figure 6). The four types of plasmonic eu-viruses were observed to have distinguishable optical resonances. Although the four types of plant viruses used are similar in size (approximately 30 nm) and identical in symmetry (T=3, where T is the triangulation number), the differences in their morphological details (as shown in the insets of Figure 6) resulted in a modulation of their optical resonances, thereby demonstrating the capability for wavelength selectivity via viral template selection. Among the four types of plant viruses, an increased proximity between protruding capsomers results in the clearer manifestation of multiple resonances in the visible range, whereas an increase in diameter generates a red shift in the optical resonance. Thus, through the selection of virus type and metal thickness, antennas with a broad range of optical resonances can be fabricated for diverse optical sensing applications.

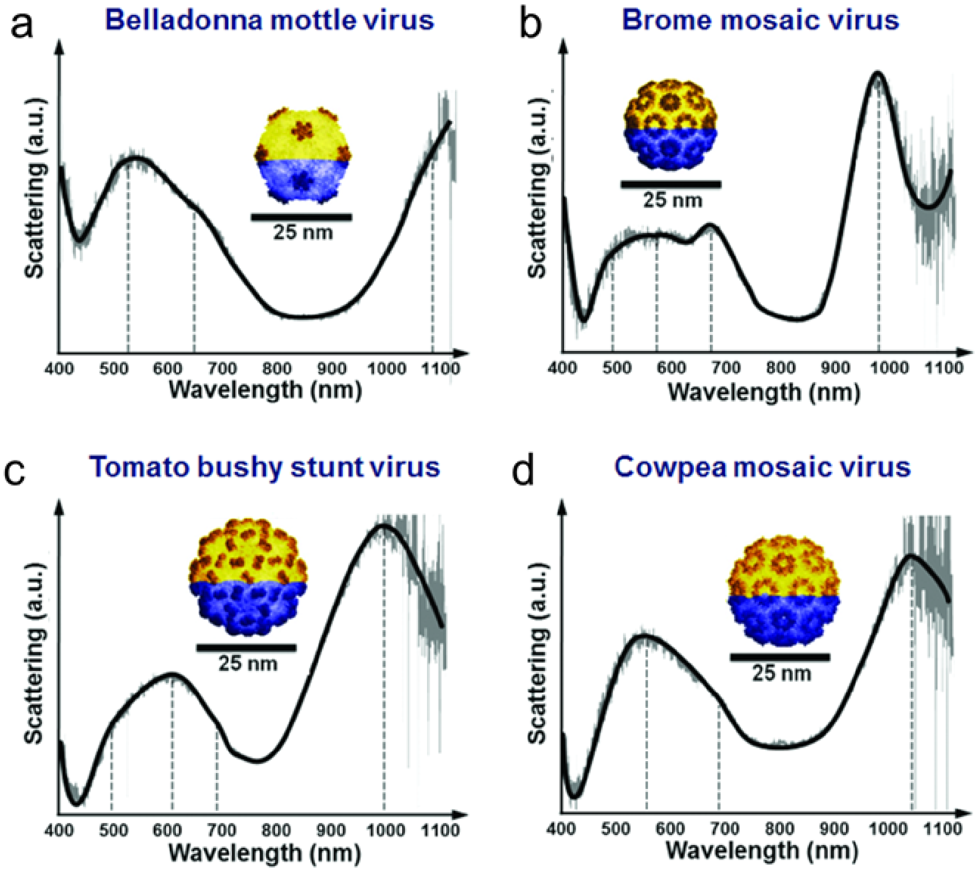

Figure 6. Measurements of the optical properties of various plasmonic eu-viruses. (a) BdMV, (b) BMV, (c) TBMV and (d) CPMV were coated with identical 5-nm gold layers via metal evaporation. The particles were prepared as single nanoparticles on a glass substrate for single-particle optical characterization. The optical measurements demonstrate variations in optical resonance frequency that are strongly dependent on the details of the capsid morphology.

III-A-3. Equilibrium morphology of plasmonic Au/polystyrene dimeric nanoparticle (Korea team)

The morphological evolution of plasmonic nanostructure in bioinspired synthesis is driven by multiple mechanisms related with various components. For the rational design and optimization of unconventional nanoantennae, the development of a reliable computational model is prerequisite, which can rigorously present a dynamic evolution of complex morphology and incorporates the multi-physics, -components, and –scales. Here we systematically studied the equilibrium morphology of metal/dielectric dimeric nanoparticle. A computational model was developed by considering the diffusion and surface energy of a metal and the interface energy between the metal and a dielectric. As a proof-of-concept, the growth of Au on a dimeric nanoparticle consisting of Au and polystyrene (PS) was considered.

***The effects of the size of the dielectric and the concentration of Au ion in the growth solution on the equilibrium morphology*:** Figure 7 shows both simulation and experimental results for the effect of the concentration of Au ion on the Au coverage for the cases of PS with three different diameters. In order to ensure a complete growth reaction, the samples for TEM measurement were collected after 3 min since no change in the solution color was observed after 3 min. From the simulation, when m is smaller than 1, the coverage increases linearly with increasing concentration of Au ion, irrespective of PS size. However, if m is greater than 1, in the case of smaller PS (60 nm), the coverage reached 100% as m is changed from 1 to 4. On the other hand, the coverage increased to only 41% even when m is increased up to 16 in the case of larger PS (200 nm). As presented in Figure 7b, the morphologies of the dimeric nanoparticle before and after growth are also compared. The experiment is consistent with the simulation. For example, from Figure 7b the coverage is expected to be increased from 17% to 38%, which is similar to the increase in the coverage estimated from the experiment (15–35%) in the case of PS with a diameter of 60 nm. Note that the rough outer surface of the Au part in the final nanoparticle in the experiment (instead of the smooth outer surface in the simulation) can be attributed to either the crystal structure of Au or the diffusion-limited growth of Au particle that are not considered in our simulation. The Au coverage of PS is a more important factor to estimate the optical property of the final Au/PS nanoparticle since it is closely related to the equilibrium morphology (i.e., nanocap, nanohalf-shell, nanocup, and nanoshell).

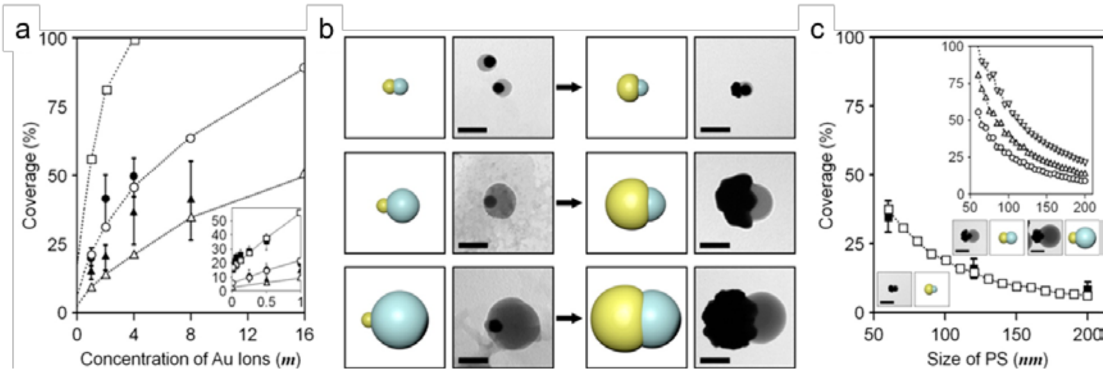

Figure 7. (a) Simulation and experimental results for the effect of the concentration of the Au ion on the Au coverage for the cases of a dielectric (PS) with three different diameters after growth of Au. Squares, circles, and triangles indicate PS with diameters of 60, 120, and 200 nm. Dotted line and void symbol represent the simulation, whereas solid symbols corresponds to the experiment. (b) Representative simulation and TEM images before and after growth. Dimeric nanoparticles were prepared by varying PS size from 60, to 120, to 200 nm. (c) Effect of the size of PS at different concentrations of Au ions on Au coverage after growth.

III-B. Results of 2nd year

III-B-1. Electromagnetic simulation and surface-enhanced Raman spectroscopy (SERS) measurements via two-dimensional hyper-branched gold nanoparticles (Korea team)

Electromagnetic field (EM) simulation was carried out using the finite-difference time-domain (FDTD) method. The EM simulation results for three kinds of 2D gold nanoparticles (i.e., 2D gold nanoparticles with primary and secondary branches, with primary branches, and without any branches) are shown in Figure 8a–c. The number of areas for strong EM enhancement (hot spot) increases with branching (Figure 8d). Strong EM enhancement is generated in small gaps between branches. In order to realize the benefit of our 2D hyper-branched gold nanoparticles, 2D gold nanodendrimers were tested for surface-enhanced Raman spectroscopy (SERS). 4-chlorobenzenethiol (CBT) was selected as a standard molecule for SERS. For the control experiment, gold nanospheres (GNS), 20 nm in diameter were tested to compare the SERS signal under the experimental conditions since GNS has a similar amount of Au atoms to the gold nanodendrimer. Figure 8e shows normalized SERS spectra of CBT from a colloidal gold nanodendrimer and GNS solutions. No apparent Raman transition is found in the Raman spectrum taken from colloidal GNS (red line in Figure 8e). In contrast, characteristic Raman transitions of CBT (assigned by asterisks, blue line in Figure 8e) are clearly observed from colloidal gold nanodendrimer solutions. This SERS enhancement from gold nanodendrimers can be attributed to many factors including a large accessible surface area without diffusion limitation, many hot spots between branches, and the wavelength of the laser.

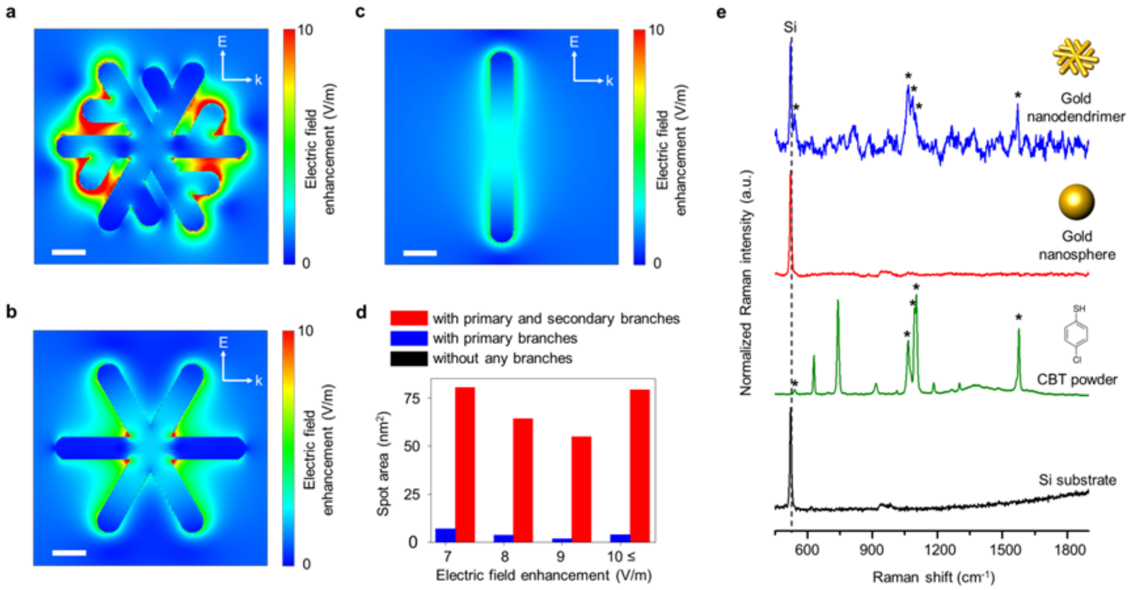

Figure 8. (a-c), Electric field enhancement for 2D gold nanoparticles with (a) primary and secondary branches, (b) primary branches only, without (c) any branches. Scale bar corresponds to 10 nm. (d), Plot of hot spot area of 2D gold nanoparticles with the enhancement factor larger than 7 (V/m). (e) SERS spectra when using colloidal gold nanodendrimer solution (blue line) and 20 nm gold nanospheres solution (red line). Raman spectra of 4-chlorobenzenethiol (CBT) powder (green line) and silicon substrate (black line). The Raman transitions of CBT are marked with asterisks (542, 1066, 1086, 1102, and 1571 cm^{-1}, respectively).

III-B-2. Molecular fingerprint detection using plasmonic eu-virus (U.S. team)

For molecular imaging using plasmonic eu-virus-based optical antennas, we demonstrated localized electronic absorption spectroscopy via a phenomenon called plasmon resonance energy transfer (PRET) and vibrational spectroscopy via surface-enhanced Raman scattering; both methods provide high sensitivity and selective molecular imaging. An enhanced electromagnetic field near the excited optical antenna can increase the intensity of vibrational modes and lead to the transfer of excitation energy to nearby molecules, yielding re-scattered signals encoding molecular fingerprints at levels far above that of the background noise. The calculations presented above indicate that the use of a plasmonic eu-virus is beneficial not only in increasing the overall radiative energy but also in creating a highly amplified electromagnetic field at multiple spots, thereby enhancing the spectroscopic results.

When the optical resonances overlap between a metallic nanoparticle and its target molecules, the molecular absorption spectra can be encoded in the scattered signals of the nanoparticle. Because plasmonic eu-viruses have larger optical cross sections than those of similar-sized nanoparticles, they offer enhanced encoding efficiency. To characterize the sensitivity of plasmonic eu-viruses for the encoding of absorption spectra, one type of plasmonic eu-virus was tested for the detection of cytochrome c (or cyt c) (Figure 9a to 9c). Various concentrations of cyt c were incubated with CPMVs coated with 5 nm of gold, and as a control, gold-coated plasmonic nanospheres (33 nm diameter polystyrene beads) were simultaneously examined. Figure 9a to 9c demonstrate that the plasmonic eu-virus allowed for more sensitive detection of the absorption spectrum of cyt c more sensitively than did the smooth plasmonic nanosphere, yielding approximately 10 fold higher magnitudes. The higher absorption encoding efficiency achieved using the plasmonic eu-virus can be understood as a result of the large number of hot spots that formed on the plasmonic eu-virus, as indicated by the simulation.

The strong electromagnetic fields that form around plasmonic eu-viruses can also permit more sensitive detection in vibrational, i.e., Raman scattering measurements because Raman scattering signals are amplified by $|E|^4$ near metallic nanostructures (here, $|E|$ is the magnitude of the electric field). For a general assessment of the efficacy of plasmonic eu-viruses in Raman detection, 1,2-bis(4-pyridyl)ethylene (BPE) was selected as the target molecule to avoid overlap between the excitation wavelength and the molecular electron transition (Figure 9d to 9f). CPMVs coated with 2 nm of gold, 33 nm nanospheres with the same gold thickness, and 33 nm nanospheres coated with 4 nm thick gold layers to achieve resonance at 785 nm were tested in 785 nm laser excitation Raman measurements. The gold-coated CPMV particles achieved clear detection at sub-picomolar concentrations of BPE, whereas the gold-coated nanospheres could detect concentrations only down to the micromolar level. A direct comparison of the detection limits indicates that the 3-dimensional folded viral capsid yielded a 10^6 fold higher sensitivity compared to the smooth nanospheres. Moreover, the Raman signals were temporally stable, with less than 10% deviation, even at the lowest concentrations. Blinking, which is commonly observed at single molecule-level concentrations, was not observed in gold-virus-based detection, which may suggest the occurrence of molecular preconcentration around the nanoscale morphology.

III-B-3. Dual function of electrokinetic concentration of charged molecules and optical detection with interfacially trapped gold nanorods at immiscible oil–water interface (Korea team)

***Computational simulation of molecular accumulation at the oleic acid–water interface*:** To estimate the extent of this molecular concentration of charged molecules at the oleic acid–water interface, a 3D dynamic model was developed. The dynamics of the concentration of R6G molecules at the interface are investigated (Figure 10) while assuming that the gradient of the electrostatic field is generated only along the $\chi3$ direction, perpendicular to the interface (Figure 10a).

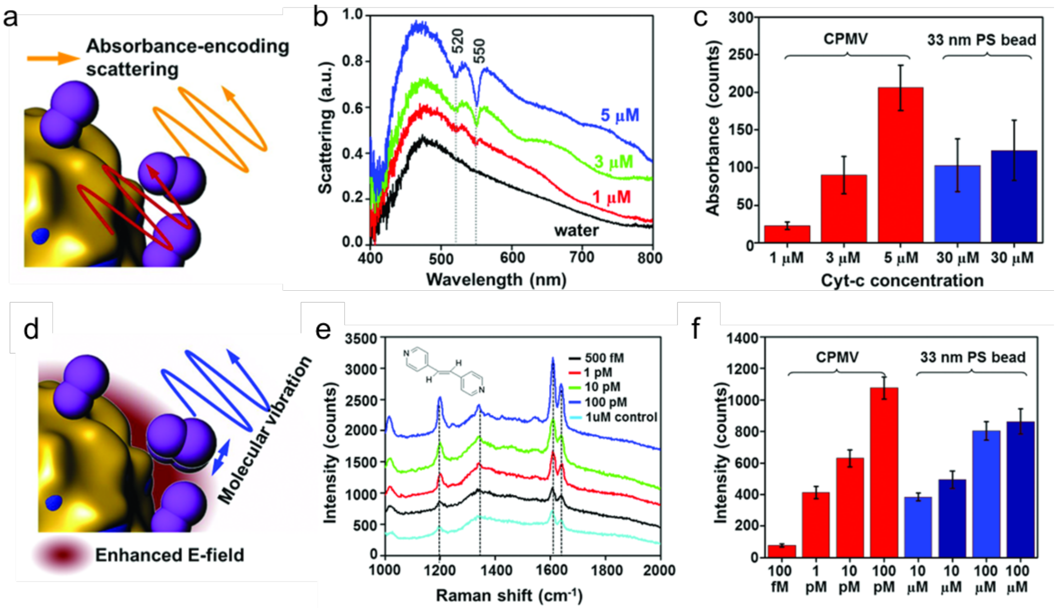

Figure 9. (a) Molecular fingerprint detection of cytochrome c via plasmonic eu-virus absorbance-encoding scattering. (b) Absorption spectra via plasmonic eu-virus (5 nm gold coated CPMV) with various concentration of cytochrome c (cyt c). (c) Comparison of the encoding efficiencies of the absorption spectra of a plasmonic eu-virus and two different plasmonic nanospheres. (d) Molecular fingerprint detection of 2-bis(4-pyridyl)ethylene by absorption via plasmonic eu-virus vibrational scattering. (e) Vibrational (or Raman) spectra via plasmonic eu-virus (2 nm gold coated CPMV) with various concentration of 2-bis(4-pyridyl)ethylene. (f) Raman scattering intensity (1615 cm^{-1}) of plasmonic eu-virus and sphere against various concentration of 2-bis(4-pyridyl)ethylene. The plasmonic eu-virus exhibited a greater sensitivity by 6 orders of magnitude.

The normalized diffusivities of R6G in water and oleic acid are 1.00 and 0.05, respectively. It is further assumed that the electrostatic potential of oleic acid is maintained at a constant during the simulation. The simulation results for 10 nM R6G are shown in Figure 10b. R6G molecules are apparently more concentrated at the oleic acid–water interface with time. Figure 10c shows a quantitative analysis of the accumulation of R6G for different initial concentrations. At the oleic acid–water interface, R6G molecules accumulate rapidly to reach a concentration that is approximately 7 times higher than the initial concentration within 2 h. The rate of accumulation of R6G decreases, with the maximum concentration being reached at about 8 h. The R6G molecule can be accumulated at the oleic acid–water interface at concentrations that are up to 10 times higher than the initial concentration in 8 h. Initially, R6G molecules are evenly distributed in the water. It is the electrostatic potential that can cause an increase in the number of R6G molecules at the interface. As the number of R6G molecules at the interface increases, a large concentration gradient is generated across the interface, leading to diffusion of R6G molecules into the oil phase, thereby reducing the number of molecules at the interface.

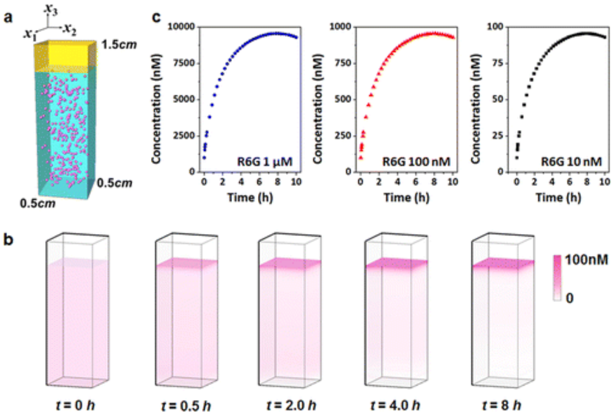

Figure 10. (a) Schematic illustration of the simulation domain considered, (b) snapshots of accumulated R6G at five different time intervals, with an initial concentration of 10 nM, (c) time-resolved plots of the concentration of R6G molecules at the oleic acid–water interface, with three different initial concentrations.

Label-free detection via surface-enhanced Raman spectroscopy (SERS)**:** To realize the benefit of this significant molecular concentration at the oil–water interface, SERS was exploited, since charged gold nanoparticles, for example, gold nanorods, could be spontaneously trapped at the interface through electrostatic interactions. Gold nanorods are positively charged due to the cetyltrimethylammonium bromide (CTAB) bilayer. SERS spectra from the oleic acid–water interface are collected as a function of time (Figure 11) for three different initial R6G concentrations (1 μM, 100 nM, and 10 nM). Among the intrinsic Raman transitions of R6G, 614 and 1513 cm^{-1} are selected as the indicator peaks for R6G, having no overlap with those of oleic acid. The SERS intensities at 614 and 1513 cm^{-1} significantly increase for all cases, and notably, the Raman peak for 10 nM R6G that was not initially visible becomes clearly detectable at 1513 cm^{-1} after 3 h (Figure 11b to 11d). For comparison, the background intensity (i.e., baseline) is also shown in Figure 11e to 11g. It should be noted that there is no increase in SERS intensity measured from the aqueous mixture of gold nanorods and R6G without the oleic acid.

III-B-4. Development of general and programmable synthetic method for liposome-metal hybrid nanoparticles (U.S. and Korea team collaboration)

We have proposed the general and programmable synthetic method for liposome-metal hybrid nanoparticles via the precise control of chemical and physical processes at liposome interface. We have successfully synthesized seven liposome-monometallic and liposome-bimetallic hybrids. Dried lipid bilayer film was hydrated with a reducing agent. The lipid bilayer vesicles with reducing agent was re-dispersed in a gold precursor solution to act as a reactor and kept overnight in a shaking incubator at room temperature for the growth of gold nanoparticle in the vesicle.

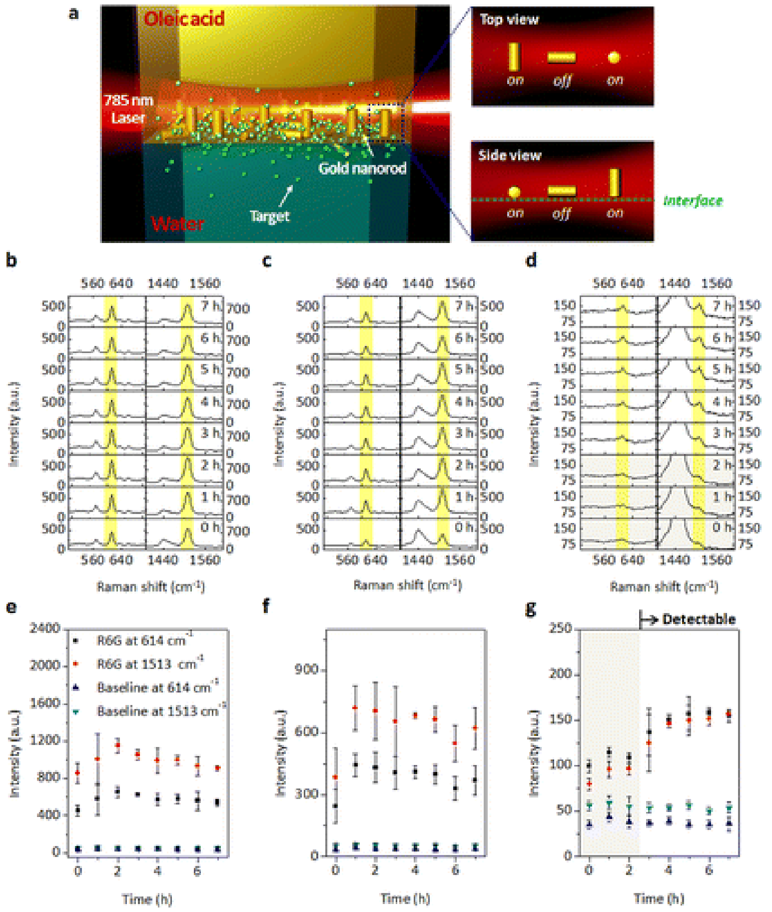

Figure 11. (a) Schematic illustration of SERS measurement at the interface. A 785 nm laser illuminates the interface. The top and side views of the interface represent possible orientations of gold nanorods and the corresponding surface plasmon resonance mode. (b to d) Time-resolved SERS spectra and (e to g) changes in peak intensities for R6G at the oleic acid–water interface are shown: (b, e) 1 μM, (c, f) 100 nM, (d, g) 10 nM R6G. Yellow bands show the indicator peaks at 614 and 1513 cm^{-1}. Each point corresponds to the average of measurements repeated three times. The error bars are the standard deviation. If the intensity measured from the interface is increased over the background fluctuation (i.e., the background intensity measured from the oleic acid–water interface without analyte) by 100 counts.

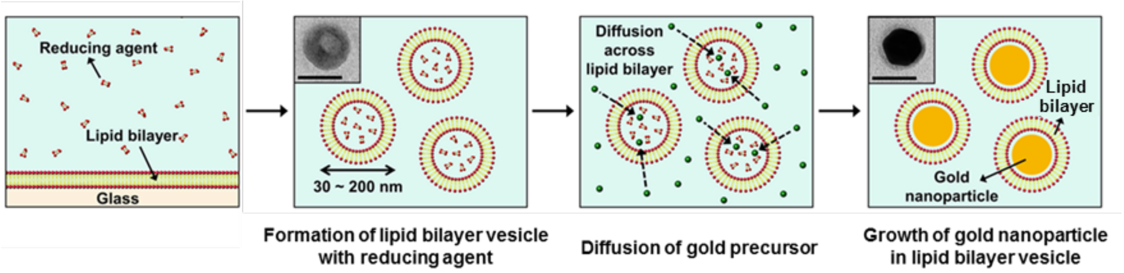

Figure 12. Schematic illustration of the synthesis of gold nanoparticles in lipid bilayer vesicle

***Morphology study of gold nanoparticles in lipid bilayer vesicle*:** Figure 13 shows the representative transmission electron microscope (TEM) images and statistical distribution of the size of lipid bilayer and gold nanoparticles in lipid bilayer. The lipid bilayer along synthesized gold nanoparticles is clearly observed indicating a growth of gold nanoparticle in lipid bilayer vesicle. The size relationships between the lipid bilayer vesicle and gold nanoparticle were also identified in TEM images and statistical analysis.

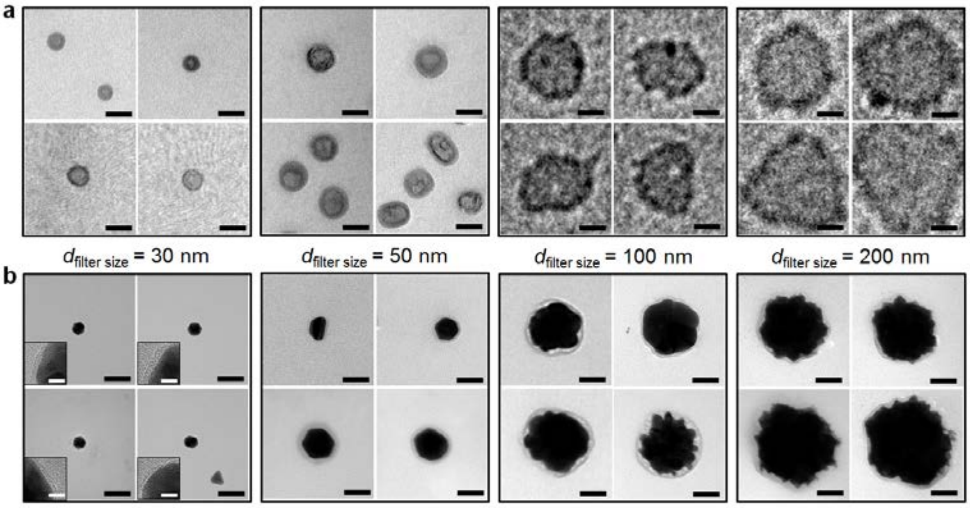

Figure 13. TEM image of (a) lipid bilayer after filtering through a filter with 30 nm, 50 nm, 100 nm, and 200 nm pore and (b) gold nanoparticles in lipid bilayer after filtering through a filter with 30 nm, 50 nm, 100 nm, and 200 nm pore

Colloidal stability study of gold nanoparticles in lipid bilayer vesicle: Gold-lipid bilayer vesicle nanoparticles were incubated with biologically solutions to study a colloidal stability of the nanoparticle. The color of the nanoparticle solution was maintained. To statistically analyze a colloidal stability, the changes in absorbance of each gold- lipid bilayer vesicle nanoparticle, bare gold nanosphere, and gold nanorod solutions were measured. The absorbance of gold-lipid bilayer vesicle nanoparticles remains unchanged for each solution (figure 14), indicating the highly enhanced stability of colloidal gold nanoparticles under biologically conditions.

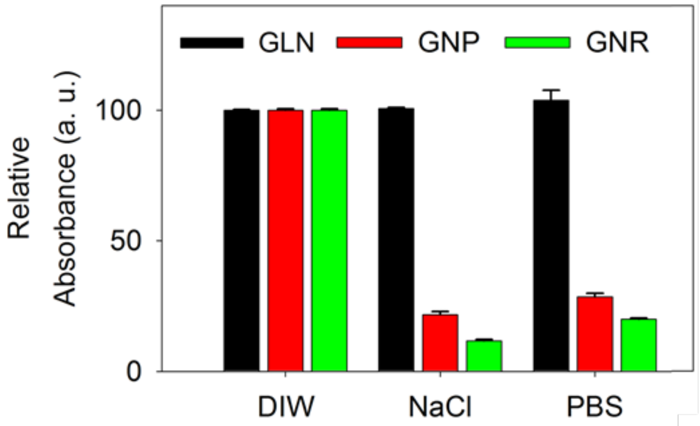

Figure 14. Colloidal stability of gold nanoparticles in lipid bilayer (GLN, black), gold nanoparticles (GNP, red) and gold nanorods (GNR, green) in deionized water, sodium chloride solution and PBS solution.

III-B-5. Spontaneous formation of three-dimensional (3D) plasmonic optical cavity on water/polymer interface (U.S. and Korea team collaboration)

Mineralization processes in nature have drawn tremendous attentions due to the ability to form inorganic-organic hybrid materials with complex patterns, hierarchical structures, and superior material's properties. The diversity of specific patterns and structures (e.g., sea sponge, sea shells, nacre, diatom, and bone) generated from the mineralization allows designing new functional materials. In this regard, we aim to develop a solution-based novel nanoplasmonic thin film process at room temperature, conceived by the bioinspired mineralization at a gradient inorganic-organic interface between water and polymeric matrix with active reagents. By controlling chemical driving forces (i.e. inorganic salt concentration and organic phase ingredient) at water/polymer interface, we successfully developed new three-dimensional (3D) functional materials and devices with nano- to micro-scale active elements.

Bioinspired photonic thin film formation at room temperature (at a liquid/polymer interface): We demonstrated the spontaneous self-formation of 3D plasmonic optical cavity structure with self-integrated plasmonic thin film layer from an ionic water droplet in liquid polydimethylsiloxane (PDMS) at room temperature. When the ionic water droplet is placed on the surface of the liquid PDMS, the water droplet is immediately surrounded by the liquid PDMS (shown in the middle image in Figure 15a). In this process, the surface tension of the water droplet is an important factor that determines the fast and spontaneous formation of a spherical cavity. As time proceeds, interfacial reduction of metal ions as well as solidification of the liquid PDMS automatically occurs without an additional step (shown in the right image in Figure 15).

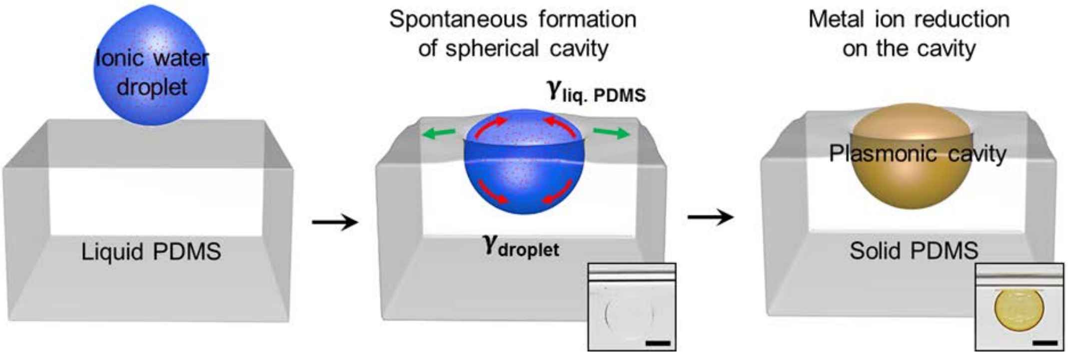

Figure 15. Schematic illustration showing one-step formation of a plasmonic optical cavity by a droplet of ionic water and sequential metal ion reduction along the surface.

When metallic nanoparticles is formed along the surface of the water cavity, Si–H groups in the curing agent act as the direct reduction reagent to form metallic nanoparticles, that is, the metal ions are diffused into the liquid PDMS and react with the residual Si–H groups, resulting in the formation of metallic nanoparticles. Therefore, as the liquid PDMS is cured, the metal ions are naturally reduced to nanoparticles, resulting in a solid spherical cavity with a self-integrated nanoparticle layer. In order to estimate the thickness of the interfacial nanoparticle layer along the surface of the cavity, cross-sectional scattering images of the interface were obtained by varying the concentration of Ag and Au ions using a dark-field microscope (Figure 16b and 16c). For both ions, as their concentrations increase (from 0.1 mM to 5 mM), the thicknesses of the resulting plasmonic nanoparticle layers gradually increase.

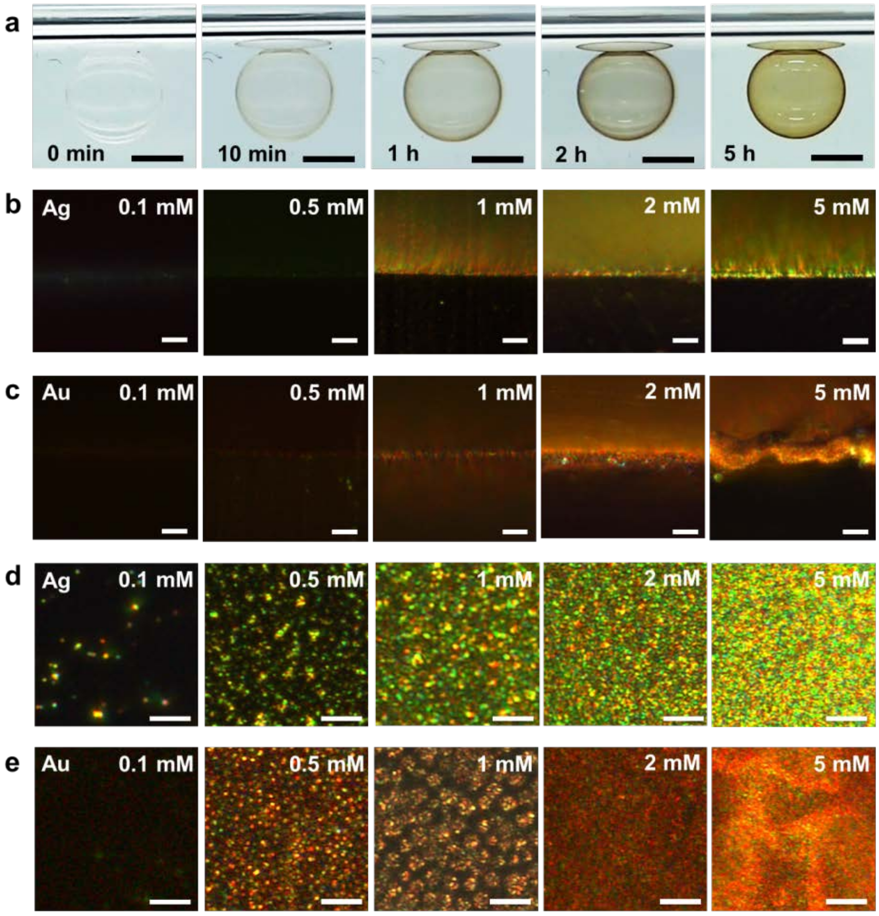

Figure 16. Self-formation of a plasmonic cavity with an interfacial layer of nanoparticles integrated along its surface. a) Time-lapse photographs of the formation of an Ag plasmonic cavity. Scale bars, 2 mm. b, c) Dark-field scattering images of cross-sectional surface of Ag plasmonic cavities (b) and Au plasmonic cavities (c) formed using different concentrations of AgNO3 and HAuCl4, respectively. Scale bars, 20 µm. d, e) Dark-field scattering images of the surface of Ag plasmonic cavities (d) and Au plasmonic cavities (e)

III-C. Results of 3rd year

III-C-1. Extension of programmable synthesis for liposome/bimetallic hybrid nanoparticle (U.S. and Korea team collaboration)

Using the solutions containing two different metal precursors (*i.e.*, Au-Ag, Au-Pd, and Au-Pt precursors, respectively), we have successfully synthesized liposome-bimetallic hybrids. Figure 17a-i) (Au-Pt precursors), Figure 17a-ii) (Au-Pd precursors), and Figure 17a-iii) (Au-Ag precursors) are the representative TEM images of the nanoparticles obtained from each solution. The nanoparticles from Au-Pd and Au-Pt precursors have a hyper-branched structure. Each magnified TEM images (d`, e`, and f` in Figure. 17b) clearly show the lipid bilayer structure around the nanoparticle. In the Energy dispersive spectrometer (EDS) spectrum of the nanoparticle obtained from Au-Ag precursors, both Au and Ag elements are obviously observed, revealing that the resulting particle is a bimetallic nanoparticle. These results confirm that our method is extended to the synthesis of the liposome/bimetallic hybrid nanoparticles. To further examine the elemental distribution of the bimetallic hybrid nanoparticles, the EDS elemental maps were obtained from each hybrid nanoparticle. Figure 17c shows TEM image of the Au-Ag hybrid nanoparticle and the corresponding elemental maps of Au and Ag, indicating the homogeneous distribution of Au and Ag element in the hybrid nanoparticle. The elemental maps of the Au-Pd hybrid nanoparticle give a similar distribution. For the Au-Pt hybrid nanoparticle, the elemental map of Au and Pt show that core of the nanoparticle is mostly Au element, whereas periphery of the nanoparticle is homogeneously mixed with Au and Pt element.

Endocytosis efficiency of gold nanoparticles in lipid bilayer vesicle: To examine endocytosis efficiency of nanoaprticle, gold-lipid bilayer vesicle nanoparticles are applied to cell. The intracellular distribution of nanoparticles was investigated through the scattering signal from the nanoparticle. As shown in Figure 18a, no significant scattering signal is observed in the purely cultured U-87MG cells. In contrast, scattering signal is clearly observed from the cells incubated with gold-lipid bilayer vesicle nanoparticles indicating the enhanced endocytosis efficiency. In addition, figure 18b clearly presented that endocytosis efficiency of lipid bilayer vesicle (GLN, green) showed much higher than that of bare gold nanoparticle (GNP, red).

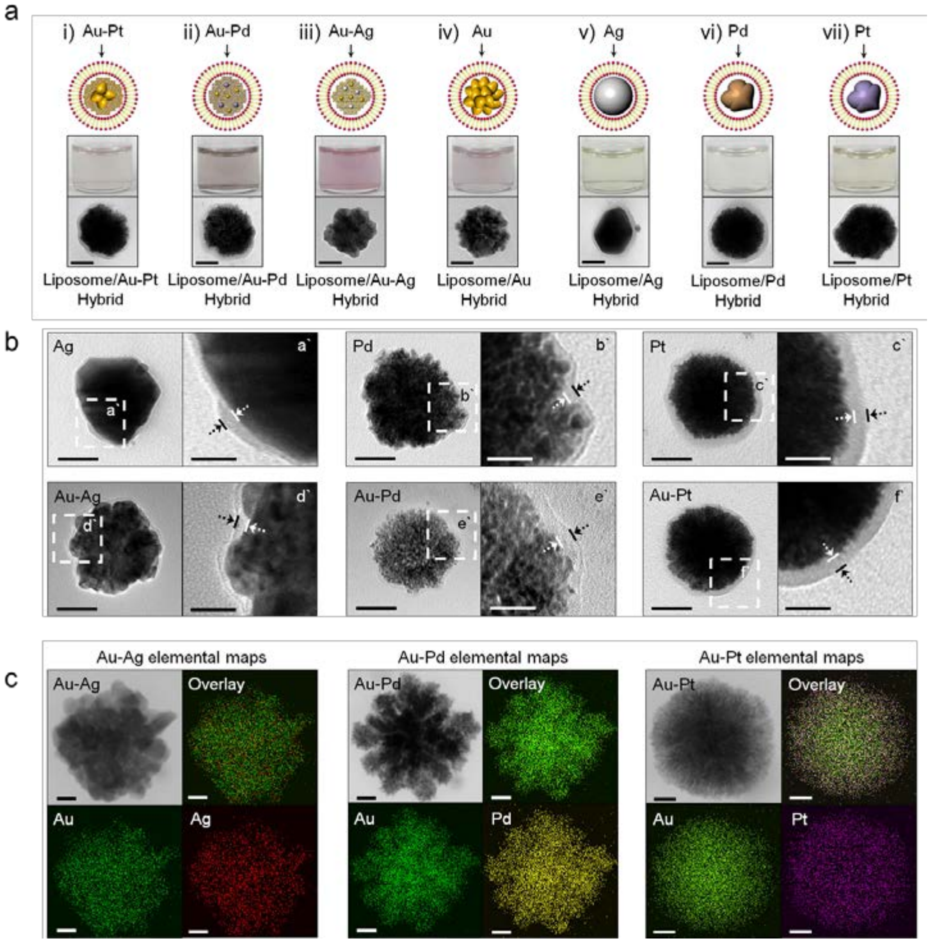

Figure 17. Programmable synthesis for liposome/bimetallic hybrid nanoparticle. (a) TEM images of seven different liposome-bimetallic (i to iii) and liposome-monometallic (iv to vii) hybrids. Each hybrids was made single or two different metal precursors i) Au-Pt, ii) Au-Pd, iii) Au-Pt, iv) Au, v) Ag, vi) Pd, and vii) Pt precursors, respectively. (b) The representative magnified TEM images of the nanoparticles obtained from each solution. Each magnified TEM images clearly show the lipid bilayer structure around the nanoparticle. (c) EDS spectrum of the liposome/bimetallic hybrids obtained from Au-Ag (left), Au-Pd (middle), and Au-Pt (right) precursors

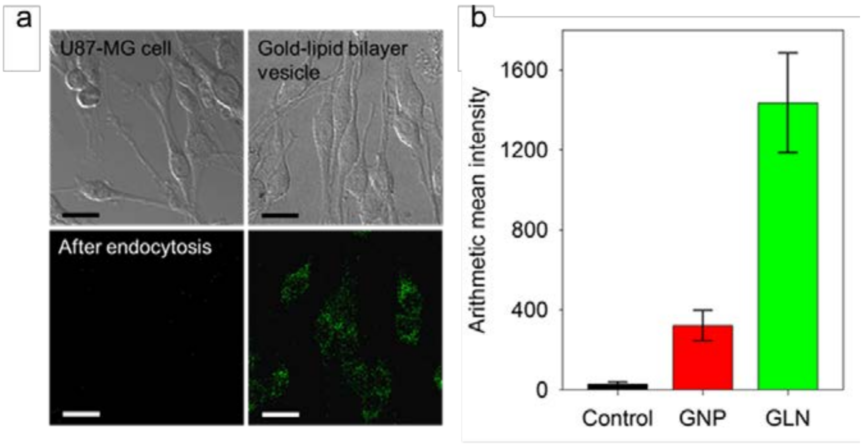

Figure 18. (a) DIC image (upper) and dark-field scattering image of U87-MG cells before (left) and after (right) endocytosis of gold nanoparticles in lipid bilayer vesicle. (b) Scattering intensity of gold nanoparticles (GNP, red) and gold nanoparticles in lipid bilayer vesicle (GLN, green) after internalization into U87-MG cells.

III-C-2. Large-scale assembly and enhanced optical properties of three-dimensional (3D) plasmonic optical cavity (U.S. and Korea team collaboration)

Through the second year research performance, we have demonstrated the self-transformation of photonic cavity with self-integrated plasmonic thin film layer from a small water droplet containing metal ions placed on an immiscible liquid at room temperature without an external force. In order for development of high performance active photonic sensor platforms, creation of closely packed cavities and a periodic array of the cavities (Figure 19a and 19b) were successfully accomplished via consecutively dropping of the metal ionic solution.

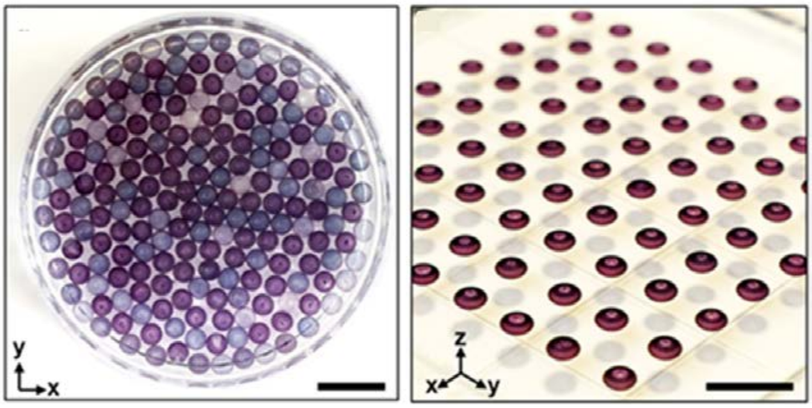

Figure 19. Large-scale assembly of 3D plasmonic optical cavity. a) Top view of close-packed Au plasmonic optical cavities. Scale bar, 1 cm. b) An array of Au plasmonic optical cavities. Scale bars, 1 cm.

To investigate the optical properties of the spherical plasmonic cavities, ray optics simulation was conducted using commercial software (COMSOL Multiphysics 5.0; Comsol, Inc.). We assumed that the Ag and Au nanoparticles formed at the interface generate continuous plasmonic films on the cavity. The simulated ray trace in the Ag plasmonic cavity is shown in Figure 20a. Results show that the accumulation of light is maximized near the bottom of the cavity and considerable increases in the accumulated ray intensity are also observed around the center and the sidewall of the cavity (Figure 20a). To estimate the near-field enhancement between the integrated nanoparticles, electromagnetic simulation was also conducted with Ag nanoparticles 154 nm in diameter and with an interparticle distance of 1 nm. The PDMS layer integrated with Ag nanoparticles shows a 300-fold higher maximum electric field intensity than that of the solid PDMS (Figure 20a). To confirm the enhanced optical performance of the plasmonic cavities we developed, the fluorescence signal from the propidium iodide (PI) in the Ag plasmonic cavity was measured by a confocal laser scanning microscopy setup with a 543 nm laser as the light source (Figure 20c). From the intensity analysis, the fluorescence enhancement increases with increasing concentration of Ag ion used in forming the Ag plasmonic optical cavity (Figure 20g). Fluorescence intensity can be maximized to 1,000 times that of the flat PDMS (an inset in Figure 20g).

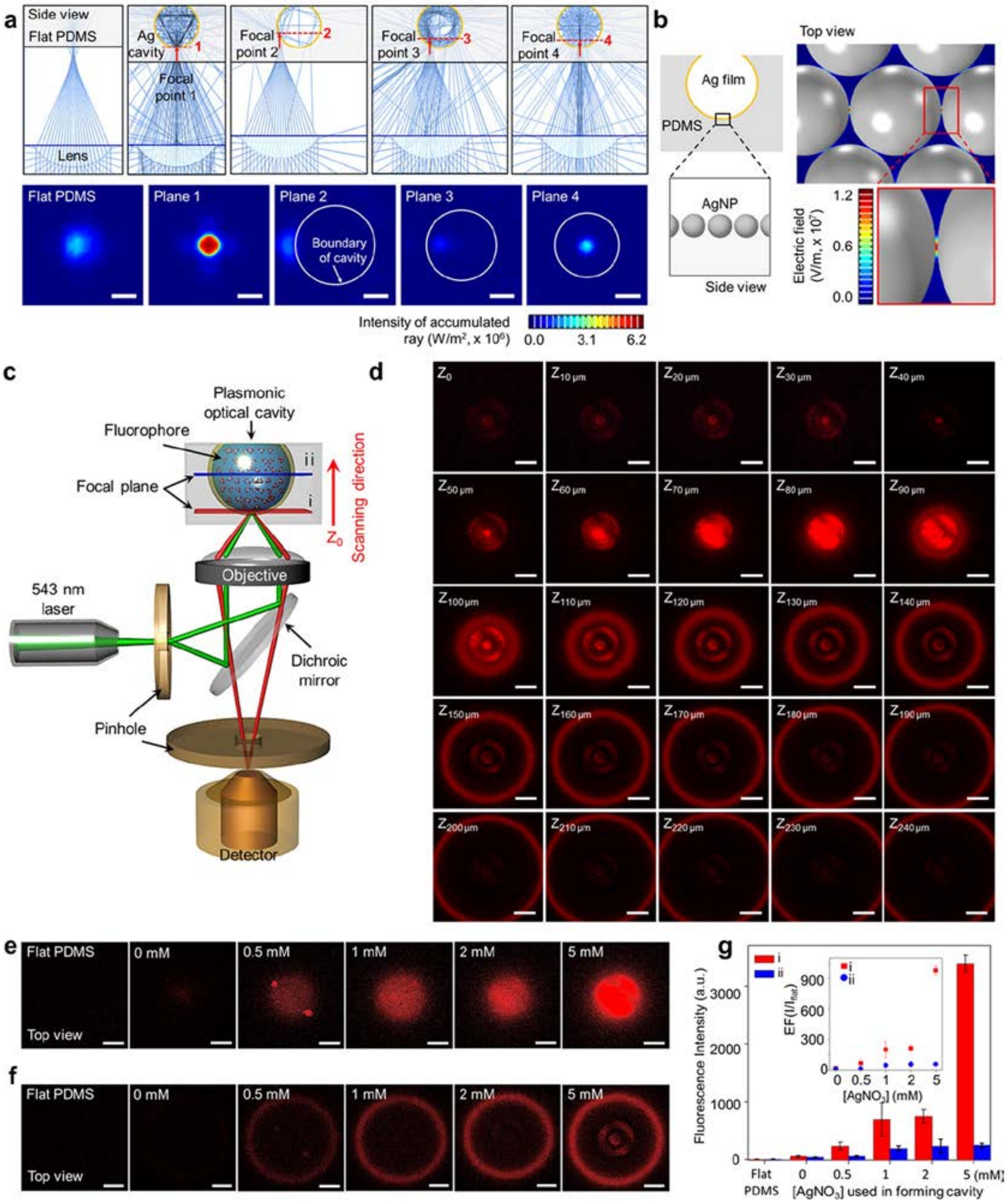

Figure 20. Optical properties of the spherical plasmonic cavity. a) Side views of the simulated ray traces in the Ag plasmonic optical cavity at different focal points (top) and representative intensity profiles of the accumulated rays for different focal planes (bottom), Scale bars, 200 μm. b) Enhanced electric field between two Ag nanoparticles. c) Confocal imaging configuration used to measure fluorescence intensity at different focal planes of the cavity. d) Representative confocal laser scanning images of a fluorophore (PI) loaded Ag plasmonic optical cavity obtained from the different focal planes. Scale bars, 200 μm. e, f) Fluorescence images of the cavities collected at the focal plane i (e) and ii (f) denoted in c. Scale bars, 200 μm. g) Plot depicting the differences in fluorescence intensities measured in different focal planes (in e and f). An inset shows a plot for fluorescence enhancement factor (EF) of each cavity compared with that of the flat PDMS.

III-C-3. Facile Preparation of Ultrasmall Void Metallic Nanogap from Self-Assembled Gold–Silica Core–Shell Nanoparticles Monolayer (Korea team)

Since nanogap between two metallic nanostructures has been demonstrated to concentrate an incident electromagnetic field into a small space, providing strong field localization. Here, we demonstrate that ca. 1–2 nm void metallic nanogaps on several substrates can be easily prepared by taking advantage of self-assembled gold–silica core–shell nanoparticles (Au@ SiO_2) monolayer at interfaces and chemical etching. Figure 21 shows schematic illustration of fabrication of ultrasmall void nanogap. Briefly, colloidal Au@SiO_2 nanoparticles in water solution were subsequently forced to assemble at hexane/water interface by the rapid addition of ethanol to the colloidal solution. The distance between Au cores that are separated by thin silica shell is further reduced to ca. 1–2 nm during chemical etching, generating ultra-small void metallic gaps.

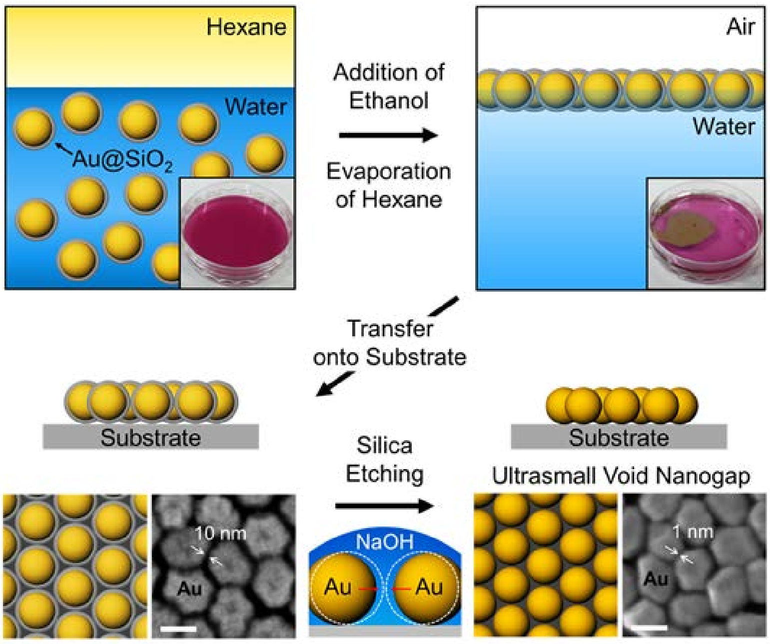

Figure 21. Schematic representation and experimental demonstration for the fabrication of ultrasmall void nanogap via kinetic control. Self-assembly of Au@SiO_2 nanoparticles at water/hexane interface by addition of ethanol into the colloidal solution, evaporation of hexane, and transfer of Au@ SiO_2 monolayer onto solid substrates (top row). Removal of thin SiO_2 shell of Au@ SiO_2 monolayer by chemical etching and concomitant decrease in gap size between Au cores (bottom row). The representative FESEM images (bottom row) show Au@SiO_2 monolayer on a glass before and after chemical etching.

To characterize Au@SiO_2 nanoparticles monolayer after being transferred onto the substrate, reflectance measurements were carried out (Figure 22). The reflectivity of Au@ SiO_2 layer on PDMS shows clear SPR band at around 590 nm, which is red-shifted by 51.0 nm compared to the SPR band of colloidal Au@SiO_2 nanoparticles in water. This shift can be attributed to both the change in the dielectric environment (i.e., from water to air/PDMS interface) and the decrease in the interparticle distance between neighboring Au@SiO_2 nanoparticles. As shown in Figure 22b, the single SPR band of Au@SiO_2 layer undergoes a transition to give two SPR bands at 581 and 786 nm as the reaction time proceeds. The two SPR bands in the visible and near-IR range can be attributed to the strong near-field coupling between the nanoparticles due to the decrease in interparticle distance upon the removal of the SiO_2 shell.

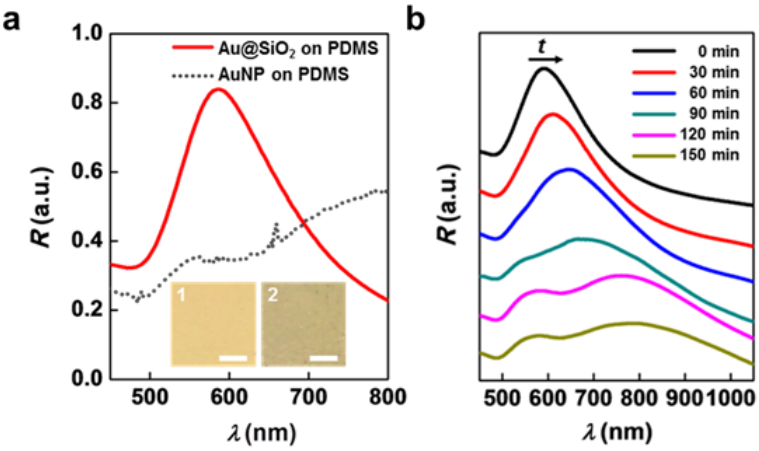

Figure 22. Characterization of Au@SiO_2 monolayer after being transferred on PDMS substrates. a) Reflectance spectra and photographs of Au@SiO_2 monolayer and citrate-stabilized Au nanoparticles layer. b) Reflectance spectra of Au@SiO_2 monolayer on PDMS as a function of chemical etching time.

To demonstrate the versatility of our method, we performed surface-enhanced Raman spectroscopy (SERS) measurements with 1,2-bis(4-pyridyl)ethylene (BPE) and adenine. SERS signal were measured from Au@SiO_2 monolayer with SiO_2 shell thickness of 5.0 nm. SERS signal of BPE at 1×10^{-9} M and adenine at 1 x 10^{-6} M is clearly visible from Au@SiO_2 monolayer after chemical etching (Figure 23).

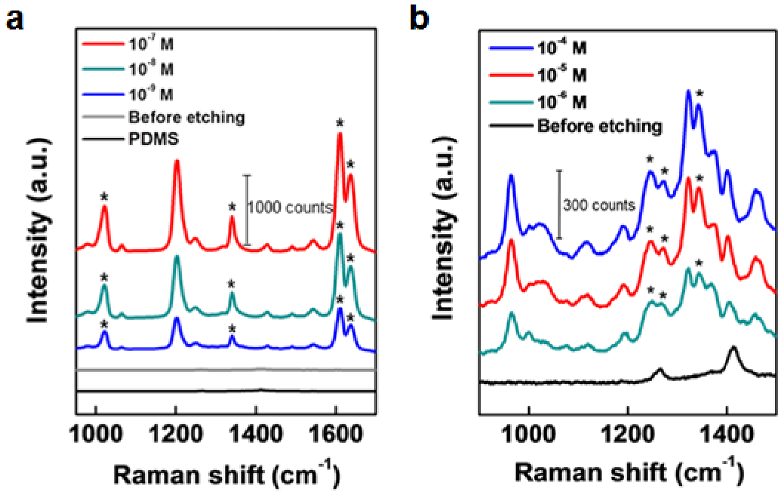

Figure 23. Surface-enhanced Raman spectroscopy (SERS) signals for three different concentrations of 10 nM, 1nM, 100 pM and 10 pM of a) BPE and b) adenine obtained from Au@SiO_2 monolayer on PDMS after chemical etching.

III-C-4. Observation of scaling behavior of chiral plasmonic resonance (U. S. team)

Chirality is one of the most significant feature in nature, as observed in collagen’s triple helix structures, DNA’s double helix from our body and, recently, it has been reported that chiral plasmonic nanostructure exhibited highly efficient interaction with an external circularly polarized light due to large dipole moment of the plasmon resonance (Figure 24). However, systematic study on the resonance of the chiral plasmonic material with circularly polarized light is not yet developed. We investigated resonance of the chiral plasmonic material with circularly polarized light with respect to the dimension of the chiral plasmonic material. We observed monotonic red-shift of first-order resonance mode of chiral plasmonic material with circularly polarized light with respect to the dimension of chiral plasmonic material, emerging of high-order resonance mode from feature size of 80 nm and polarity inversion of circular dichroism in even-numbered eigenmodes. Finite-difference time-domain simulation demonstrated dipolar and quadrupolar resonance of chiral plasmonic material and is matching with our experiment result. We believe that our finding of dimensional effect on resonance mode of chiral plasmonic nanostructure could broaden the understanding of plasmonic circular dichroism behavior.

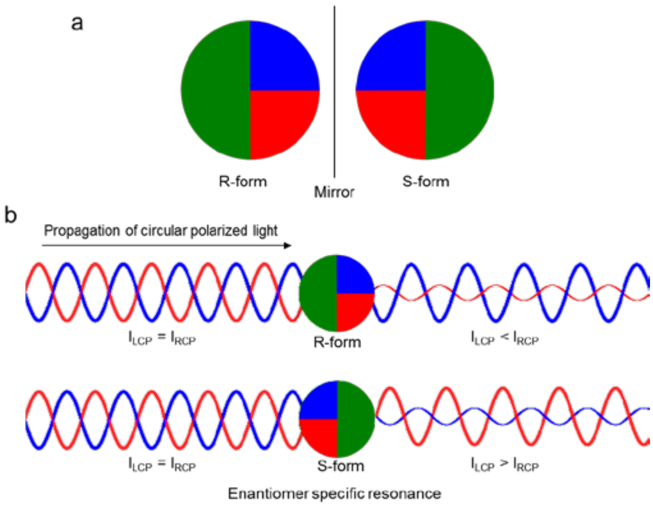

Figure 24. Schematic illustration of strong optical resonance of chiral plasmonic nanostructure with circular polarized light. (a) Superimposability of mirror image of chiral plasmonic nanostructure enantiomers. (b) Enantiomer specific resonance of chiral plasmonic nanostructure with circular polarized light.

Fabrication of chiral plasmonic nanostructure: We prepared hexagonally un-packed array of chiral plasmonic nanostructure to observe chiroptical resonance spectrum originated from the chiral plasmonic nanostructure and suppress undesired signal originated from randomness in the structure, for example distortion of chiral plasmonic structure on the region of aggregated nanoparticle template or shadowing effect, where distance between two adjacent nanoparticle template is too short. Polystyrene nanoparticle is hexagonally packed on the substrate in wafer scale by interface trapping method. By modulating surface tension of aqueous solution, hexagonally packed monolayer of polystyrene nanoparticles with a diameter ranging from 100 nm to 500 nm is trapped between water/air interface. Then, hexagonally unpacked monolayer of polystyrene nanoparticle is transferred on the silicon wafer or glass substrate. Then, hexagonally un-packed array of polystyrene template is prepared by applying oxygen plasma. Diameter of polystyrene template and gap between adjacent polystyrene is controlled by varying dimension of polystyrene nanoparticle and modulating time and power of oxygen plasma treatment. Then chiral plasmonic nanostructure is defined by sequential angle deposition of Au layer on the hexagonally un-packed array of polystyrene template. First layer (red color in figure 25a) is deposited at certain angle (α=0) with an inclined angle (φ) of π/4. Then, the second layer (green color) is deposited at α=+π/2 (right-handed structure) or α=-π/2 (left-handed structure) with φ=π/4.

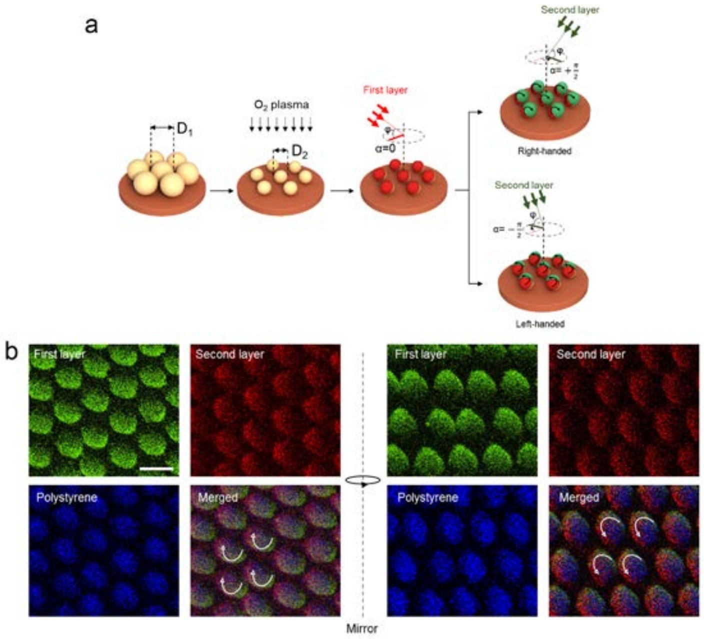

Figure 25. (a) Schematic illustration describing fabrication of left-handed and right-handed chiral plasmonic nanostructure array. Polystyrene nanoparticle is hexagonally packed on the substrate in wafer scale by interface trapping method. Then diameter of polystyrene is reduced to produce hexagonally un-packed array of polystyrene nanoparticles by applying oxygen plasma. Then first layer (red color) is deposited at certain origin of azimuthal angle (α=0) with an inclined angle (φ) of π/4. Then, the second layer (green color) is deposited at α= -π/2 (right-handed structure) or α= -π/2 (left-handed structure) with φ=π/4. (b) STEM-EDS mapped image of left-handed (left) and right-handed (right) form of chiral plasmonic nanostructure array.

Scaling behavior of chiral plasmonic resonance: Dimensional effect on the resonance of chiral plasmonic material with circularly polarized light is depicted in figure 26. Hexagonally un-packed array of chiral plasmonic nanostructure with various dimension (20, 40, 80, 160, 240 and 320 nm) was prepared on the SiO_2 substrate and circular dichroism (CD) spectrum is investigated. Note that circular dichroism is defined as (ALCP-ARCP). In general, organic molecules exhibits circular dichroism intensity in 10 mdeg range, but chiral plasmonic nanostructure demonstrated in 1000 mdeg range. This result suggests that chiral plasmonic nanostructure is efficiently coupling to chiral plasmonic light and is expected to utilize in manipulation or focusing of circularly polarized light. Red line in figure 26a is CD spectrum from left-handed plasmonic nanostructure (Deposit second Au layer o $\alpha=-\pi/2$) and blue line in each graph is CD spectrum from right-handed plasmonic nanostructure (Deposit second Au layer o $\alpha=+\pi/2$). Circular dichroism of same dimension, but opposite handness exhibited similar shape with opposite polarity as observed by organic enantiomers. Band in red color in each graph denotes on-set of first order mode of chiral plasmonic resonance, green color denotes the second order and the blue color denotes the third order mode of chiral plasmonic resonance. First order mode of chiral plasmonic resonance is exhibited at c.a. 640 nm when dimension of chiral plasmonic nanostructure is 20 nm and is monotonically red-shifted as dimension of chiral plasmonic nanostructure is increased. Finally, first order mode of chiral plasmonic resonance is disappear in our spectral window (200 to 900 nm) when the dimension of chiral plasmonic nanostructure is exceed 160 nm. As observed by plasmon resonance under linearly polarized light, we hyphothized that first order mode is originated from dipolar chiral resonance mode and we are pursuing to explain the result by using electromagnetic simulation. We believe that our finding of dimensional effect on resonance mode of chiral plasmonic nanostructure could broaden the understanding of plasmonic circular dichroism behavior.

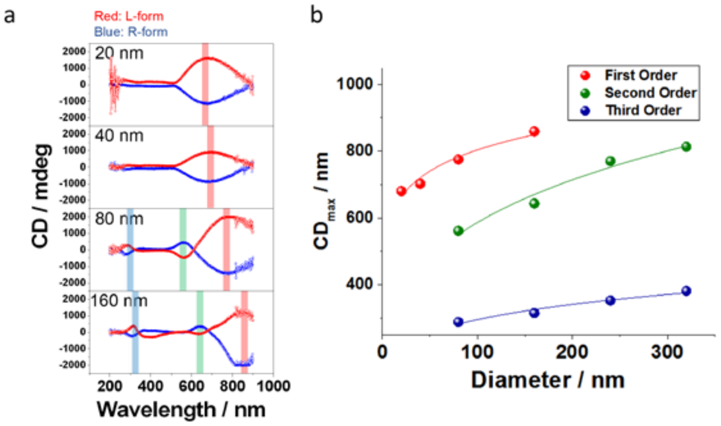

Figure 26. (a) Circular dichroism (CD) spectrum of chiral plasmonic nanostructure with various dimensions. Red line in each graph is circular dichroism or g-factor spectrum from left-handed plasmonic nanostructure and blue line in each graph is circular dichroism or g-factor spectrum from right-handed plasmonic nanostructure. Both lines are in similar shape with opposite polarity. Band in orange color denotes on-set of first order mode of chiral plasmonic resonance and band in sky-blue color denotes on-set of second order mode of chiral plasmonic resonance. (b) Plot of the size of chiral plasmonic nanostructure array dependent CD peak.

III-D. Results of 4th year

III-D-1. Ultrafast and Precise Identification of Waterborne Pathogens by Two-dimensional Nanoplasmonic Optical Antennas (U.S. and Korea team collaboration)

Waterborne pathogens related diseases are caused by pathogenic microorganisms such as bacteria, virus, and parasites that are transmitted through contaminated water. It is a serious global burden which is estimated to cause more than 2.2 million deaths per year and about 1.5 millions of these deaths are children. For the prevention of the waterborne pathogens related diseases proliferation, development of ultrafast and precise identification methods for waterborne pathogens is essential. Due to the conventional detection methods of waterborne pathogens has been based on selective culture and cell-counting technique, these methods are limited by their long response time (1-3 days), low sensitivity, and low selectivity. In order to overcome these problems and accomplish ultrafast and precise identifications of waterborne pathogens, our team has designed a novel integrated diagnostic platform composed of three steps: (1) 2D interfacial assembly of plasmonic nanostructures which possess excellent physical properties, such as ultrafast optical response, active optical modulation (i.e. near-field and far-field) on bacteria surface, (2) pre-concentration of bacteria with plasmonic nanostructures on 2D plasmonic nanoporous membrane via hydrodynamic trapping, and (3) integrated nanopore surface-enhanced Raman spectroscopy (iNSERS) measurement from the 2D nanoplasmonic optical membrane. Owing to the nanopore geometry, constructive interference would result in strong near-field enhancement between GNPs as well as GNP and 2D nanoplasmonic optical membrane near the nanopores (Figure 27).

Self-assembly of GNPs on bacteria surface and fabrication of Plasmonic nanopore membrane: For the self-assembly of GNPs on bacteria surface, the surface of GNPs was modified with hydroxylamine hydrochloride (HAHC) which was used to reduce the strong negative surface charge. Then, HAHC-modified GNPs with a diameter of 20 nm were mixed with Escherichia coli (*E. coli*). After mixing, *E. coli* was densely covered with GNPs (Figure 28a). As shown in Figure 28b, absorbance spectra of E.coli suspension shows that SPR band slightly red-shift ($\Delta\lambda = 4$ nm) and another broad SPR band appears in the near-infrared (NIR) region after mixing.

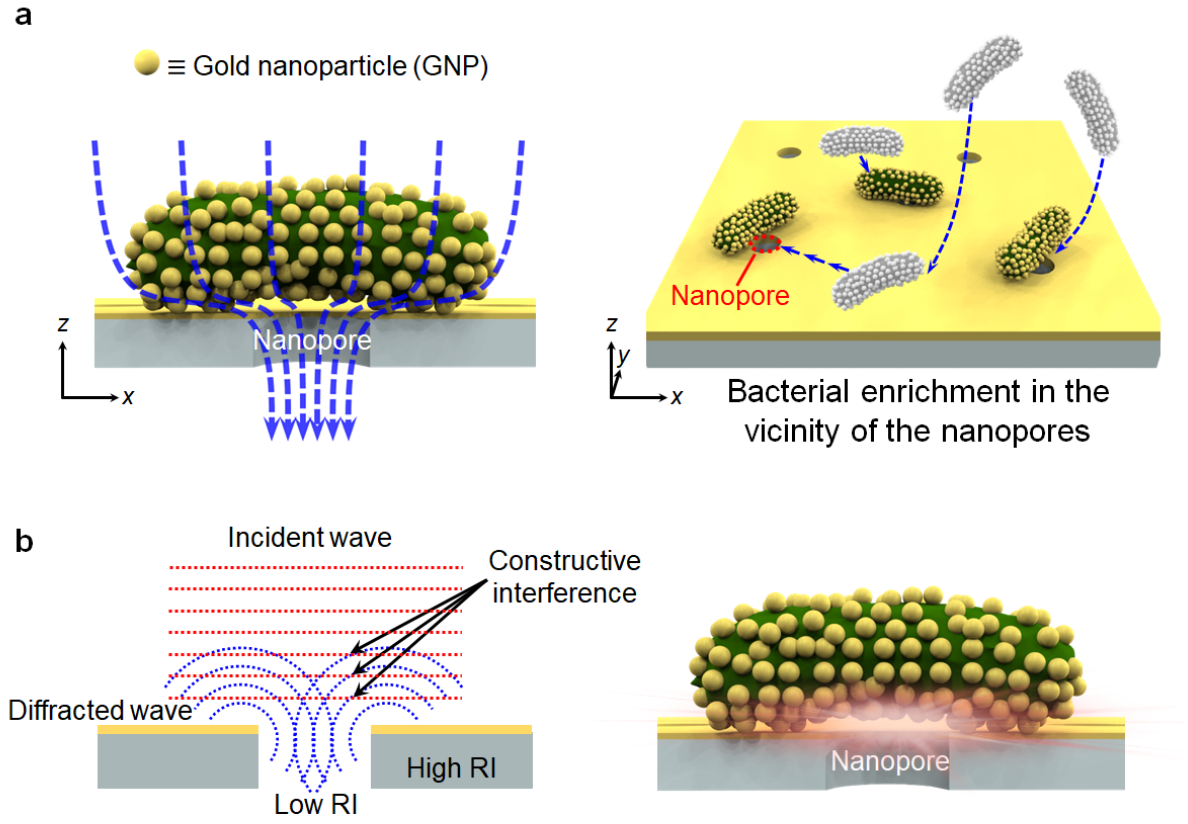

Figure 27. Plasmonic bacteria on nanopore membrane. (a) Schematic illustration of hydrodynamic trapping of plasmonic bacteria on nanopores. Due to the hydrodynamic force on the bacteria surface, GNP-assembled bacteria are forced to move along the flow and located above the nanopore. (b) Schematic illustration of constructive interference between incident light and light diffracted at fringe of the nanopore (left). The constructive interference leads to strong near-field enhancement between GNPs as well as GNP and gold thin film around the nanopores (right).

This indicates that surface plasmons of GNPs coupled with each other as the interparticle distance decrease after mixing. These results show that HAHC-modified GNPs are densely self-assembled at the surface of bacteria. The zeta-potentials of E. coli, HAHC-modified GNPs, and citrate-capped GNPs were -44.2 ± 10.3, -10.9 ± 7.8, and -178.6 ± 6.4 mV, respectively (Figure 28c). This indicate that the driving force the self-assembly of GNPs on bacteria is electrostatic interaction between the surface of *E. coli* and HAHC-modified GNPs. Plasmonic nanoporous membrane for the hydrodynamic trapping is fabricated through two sequential deposition of metal (gold) and dielectric (SiO_2) layer. The deposition of gold thin film and SiO_2 layers was demonstrated by reflectance measurement and energy-dispersive X-ray spectroscopy (EDS) (figure 28d). The overall intensity of reflectance spectrum of gold film is reversely proportional to the SiO_2 film thickness because the SiO_2 layer acting as anti-reflective agent. In addition, the EDS elemental maps show that as the SiO_2 film thickness increases, Si atoms become more abundant on the membrane.

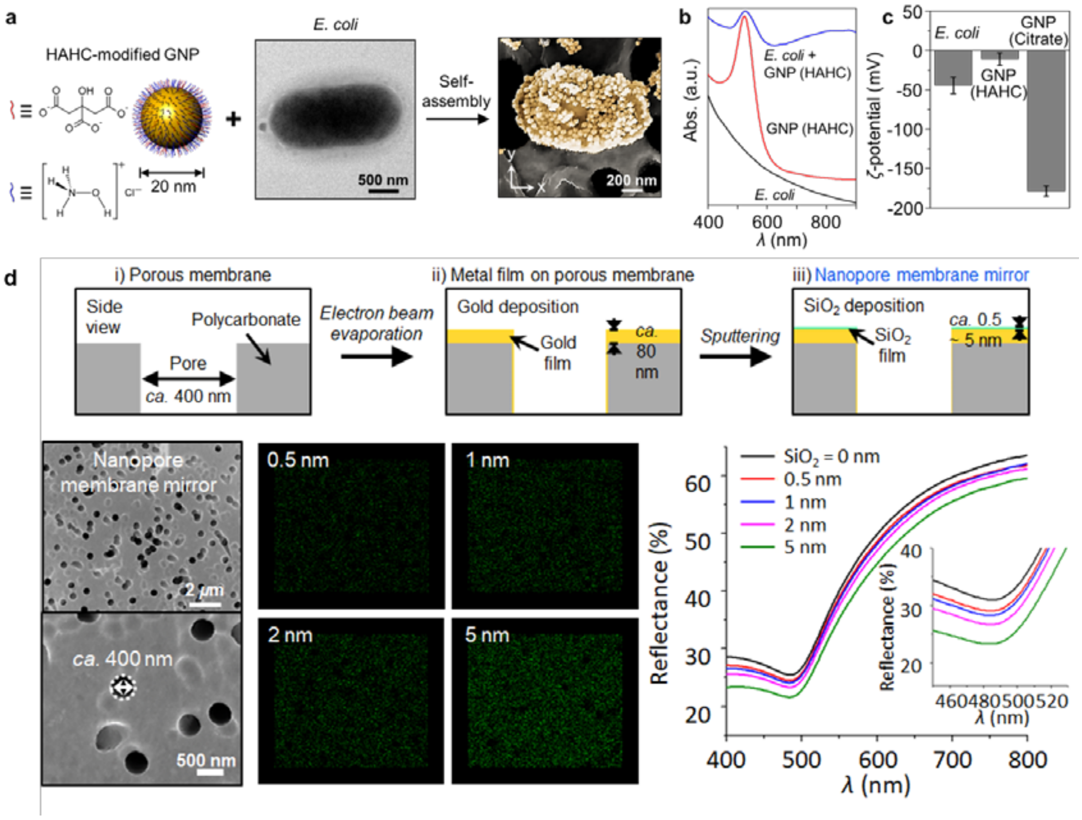

Figure 28. Self-assembly of gold nanoparticles on bacteria and fabrication of nanoporous membrane. (a) Self-assembly of hydroxylamine hydrochloride (HAHC)-modified gold nanoparticles (GNPs) on E. coli surface. Schematic illustration of HAHC-modified GNPs, transmission electron microscope image of E. coli, and representative scanning electron microscope (SEM) image of GNP-assembled *E. coli*. (b) UV-vis spectra of E. coli suspension, HAHC-modified GNP solution, and mixed solution of HAHC-modified GNP and *E. coli*. (c) Zeta-potentials of E. coli, HAHC-modified GNP, and citrate-capped GNP. (d) Schematic of fabrication process of the nanoporous mirror membrane via two steps serial deposition; electron beam evaporation for gold thin film and sputtering for SiO2 layer. Representative SEM image of the nanoporous membrane. Energy-dispersive X-ray spectroscopy (EDS) element mapping and reflectance spectra of plasmonic nanoporous membrane.

Electromagnetic (EM) simulation of plasmonic bacteria on nanopore: In order to investigate the optical properties of GNP-assembled bacteria on nanoporous mirror membrane, wave optics simulation was carried out by using the commercial electromagnetic simulation package (COMSOL Multiphysics). Figure 29a shows EM field distribution corresponding to the dotted squared box in the scheme depending on different types of membrane (polycarbonate (PC) membrane without pore, SiO_2 and gold thin films on PC membrane without pore, and SiO_2 and gold thin films on PC membrane with nanopore). In the EM simulations, we calculated the local electric field enhancement ($|E|/|E_0|$) from the ratio of near-field ($|E|$) and the incident field ($|E_0|$). The EM field distribution images show that when SiO_2/Au are on PC membrane, overall intensity of local electric field enhancement is increased, especially in the space between SiO2/Au and GNP. Furthermore, when nanopore is introduced to SiO_2/Au on PC membrane, the enhancement remarkably increases. As shown in the low magnification EM field distribution (Figure 29b), we suppose that this increase is due to the constructive interference between diffracted light at the fringe of pore and incident light. In order to examine the effect of SiO_2 thickness on the near-field enhancement, EM simulation was conducted with different thickness of SiO_2 film (from 0 to 5.0 nm). As the SiO_2 thickness decreases, the maximum local electric field enhancement increases exponentially whereas the value drastically decrease when the SiO_2 thickness becomes 0 nm. This inverse relationship between the SiO2 thickness and the near field enhancement is due to the decrease in plasmon coupling intensity as the distance increases.

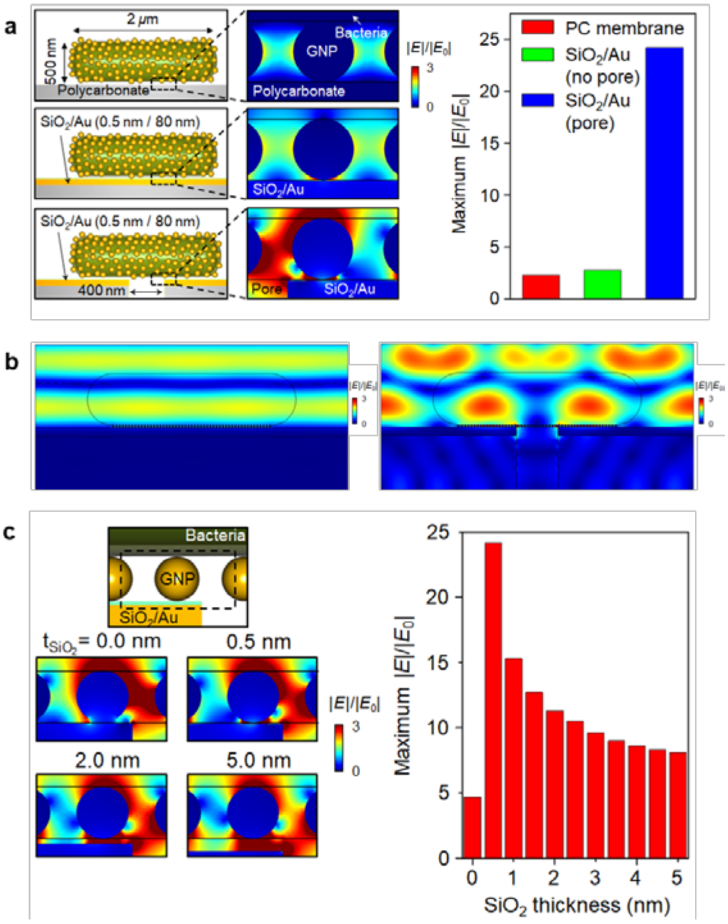

Figure 29. Electromagnetic field simulation of GNP-assembled bacteria on nanoporous membrane. (a) Schematics of GNP-assembled bacteria on (top) PC membrane, (middle) SiO_2/Au coated PC membrane, and (bottom) SiO_2/Au coated porous PC membrane and corresponding cross-sectional view of electromagnetic simulation results. Calculated maximum normalized electric field amplitude ($|E|/|E_0|$) with respect to the condition of membrane. (b) EM simulation results in low magnification. EM simulation of plasmonic bacteria on PC membrane without pore (left) and with pore (right). (c) EM simulation results with different thickness of SiO_2 layer. Schematic illustration and corresponding EM field distribution images with SiO2 thicknesses (0, 0.5, 2.0 and 5.0 nm). Calculated maximum $|E|/|E_0|$ with respect to SiO_2 thickness.

Raman measurement results of GNP-assembled bacteria on nanoporous membrane: Plasmonic bacteria on nanoporous membrane was applied to bacteria detection of SERS. *P. aeruginosa* and *E. coli*, typical waterborne pathogens, were selected for the demonstration. In order to evaluate the sensitivity and detection time, plasmonic nanoporous membrane was integrated into fluidic channel. After conjugating GNPs on *E. coli*, GNP-assembled *E. coli* was introduced into the microfluidic channel and they were enriched onto the nanoporous membrane. Raman signal was sequentially measured (Figure. 30a). As the SiO_2 thickness decreases, the maximum Raman intensity increases in accordance with Electromagnetic field simulation results. When the SiO2 thickness was 0.5 nm, the Raman intensity showed the maximum value (Figure 30b). Figure 30c shows Raman spectra of two bacteria. Three Raman transitions that can be assigned as Raman signal from bacteria were observed. The three Raman transitions, 717 cm-1, 958 cm-1, and 1351 cm-1, can be assigned to glycosidic ring mode, ν(CN), and ν(COO-), respectively. The Raman spectra show that the two species cannot be differentiated because both bacteria are gram-negative bacteria, thus they have similar outer membrane structure which is responsible for the SERS signal. Figure 30d shows Raman spectra with different concentrations of *E. coli*. Raman spectra were analyzed based on the Raman transition of $\nu(COO^-)$ and the limit of detection is found to be 10^2 cells/mL. Regarding the detection time for the microfluidic platform, the total detection time is ca. 10 min which contains GNP conjugation, bacterial enrichment, and detection step.

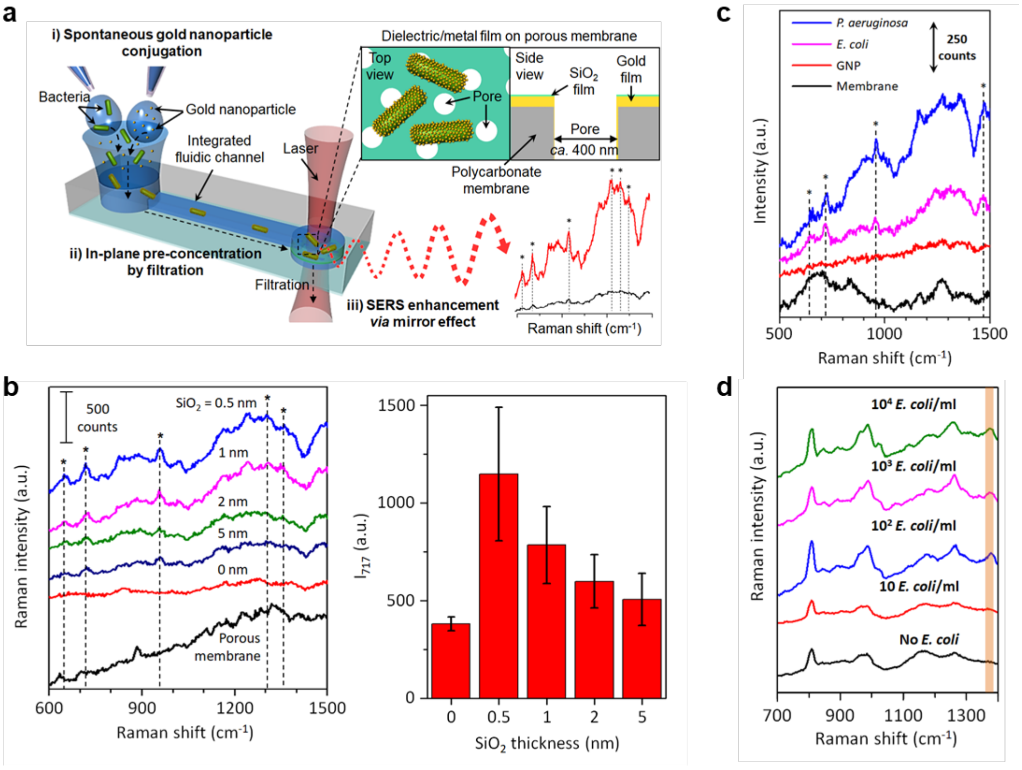

Figure 30. Raman measurement results of GNP-assembled bacteria on nanoporous membrane (a) Schematic illustration of nanoporous membrane-integrated fluidic channel (b) Raman measurement results of GNP-assembled E.coli on membrane with different SiO_2 thicknesses (left) and Raman intensity at 717 cm^{-1} with respect to SiO2 thickness (c) Raman spectra of nanoporous membrane with no bacteria (black), only GNPs (red), GNP-assembled *E. coli* on nanoporous membrane (purple), and GNP-assembled *P. aeruginosa* on nanoporous membrane (blue). (d) Raman spectra of GNP-assembled *E. coli* with different concentrations.

III-D-2. Asymmetric Nanocrescent Antenna on Upconversion Nanocrystal (U.S. team)

Our objective in this work is the development of asymmetric nanocrescent antenna on upconversion nanocrystal (ANAUs) consists of the plasmonic antenna in nanocrescent shape on the upconversion nanoparticle for enhanced frequency upconversion efficiency with asymmetric far-field radiation pattern. This new type of ANAUs is expected to impact on various applications, including ultra-high sensitive biosensors and chip applications, in vivo gelation for stem cell delivery, and high efficient phototherapies. To achieve our objective, we defined our specific aims as follows: 1) Rational design of the structure of ANAUs for enhanced frequency upconversion efficiency with asymmetric far-field radiation pattern. 2) Computationally simulate the interaction of the ANAUs with electromagnetic radiation: Near-field simulation for nanofocusing of electromagnetic wave and far-field simulation for asymmetric radiation pattern of the frequency upconverted emission. 3) Fabricate ANAUs with >10 times higher enhanced frequency upconverted emission per particle. 4) Demonstrate asymmetric frequency upconverted emission from a single particle.

The design strategy of the asymmetric plasmonic antenna: Figure 31 shows the design strategy of the asymmetric plasmonic antenna for the nanofocusing of excitation light and concentration on frequency upconverted emission. We designed asymmetric nanocrescent antenna on upconversion nanocrystal (ANAUs), which consist of the asymmetric plasmonic antenna in a nanocrescent shape on the upconversion nanoparticle. Nanocrescent antennae act as receiving antennae, which are nanofocusing excitation light to enhance the excitation of the frequency upconversion nanoparticle (UC) (Figure 31c). As validated in various models, including transformation optics, finite-difference-time-domain (FDTD) and finite element method (FEM) modeling, the plasmonic nanocrescent structure focusing excitation light on the nanoscale regime, especially a singular tip region, by excitation in the body of the crescent then propagating toward the tip region as SPP. Propagation of SPP toward the tip region of the nanocrescent is not dependent on the location of the excitation as demonstrated by an incident angle dependent near-field electric field distribution simulation (Figure 31b). Therefore, the plasmonic nanocrescent structure has the potential to efficiently excite UC near the tip region. Moreover, in the meantime, nanocrescent antennae act as emitting antennae for frequency upconverted emission by modulating the far-field radiation profile (Figure 31d). Without the nanocrescent antennae, UC exhibits a symmetric emission pattern due to the anisotropic geometry of UC, but when it is assembled with nanocrescent antennae, the asymmetric emission is exhibited due to the interaction of radiated emission with the nanocrescent antenna.

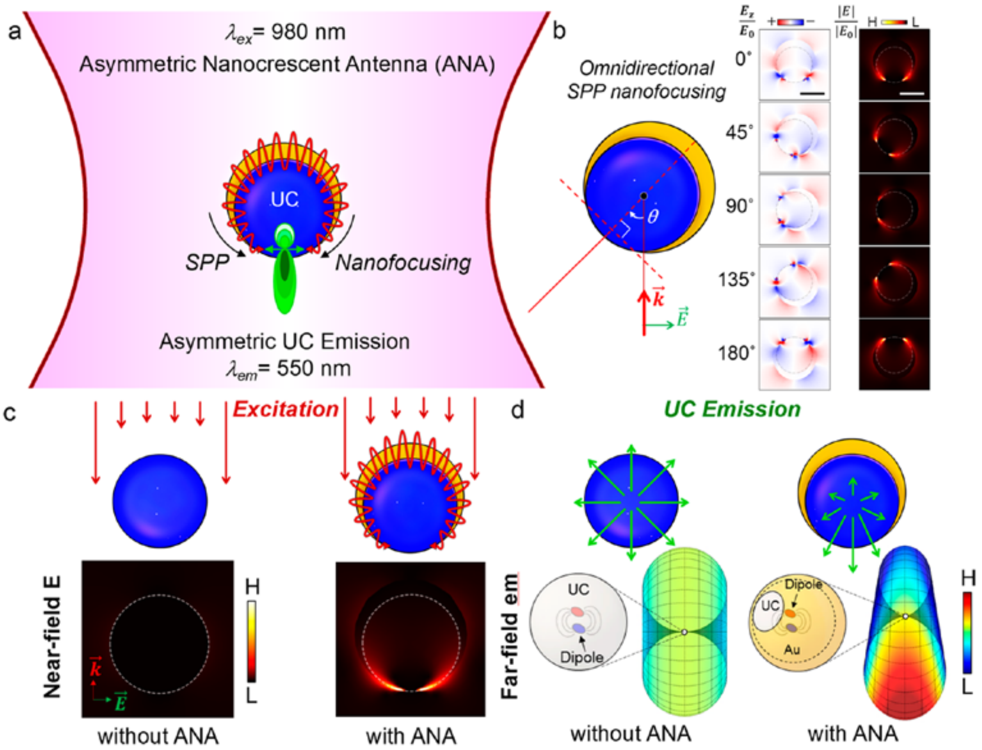

Figure 31. The design strategy of the asymmetric plasmonic antenna. (a) Schematic illustration of nanofocusing of excitation light and concentrating upconversion emission of asymmetric nanocrescent antenna on upconversion nanocrystal (ANAUs), which consist of nanocrescent-shaped asymmetric plasmonic antennae on the upconversion nanoparticle (UC). (b) Schematic diagram for incident angle-dependent near-field electric field distribution around an ANAU. The direction of the propagating electromagnetic field (k) is fixed at 0˚ and location of the tip of the nanocrescent is rotated by angle θ from 0˚. (Left lane) Near-field distribution of z-component (Ez) and (Right lane) norm (|E|/|E0|) of the electric field in the vicinity of an ANAU with various incident angles (θ = 0˚, 45˚, 90˚, 135˚, and 180˚). (c) Schematic diagram and representative simulation of nanofocusing of excitation light of ANAUs with (left) and without (right) nanocrescent antenna. In the simulation, electric field norm distribution under the background TE polarized plane wave propagating along the direction of the k-vector in the diagram is depicted. (d) Schematic diagram and representative simulation of asymmetric emission of ANAUs with and without nanocrescent antennae. In the simulation, the far-field radiation pattern (energy flux density) of a z-polarized point dipole without (left) and with (right) nanocrescent antenna is depicted.

Optimization of nanofocusing of excitation light: Spherical UCs consisted of sodium yttrium fluoride ($NaYF_4$) as a host matrix, which was doped with Yb^{3+} and Tm^{3+} using the thermal decomposition method. Synthesized UCs have a spherical shape with uniform size distribution (Average diameter: 70.4 nm), which exhibit a perfect hexagonal close-packed (HCP) structure depicted by a selected area electron diffraction (SAED) pattern and a single crystalline structure with a uniform lattice distance of 0.5 nm in high-resolution (HR) TEM image (Figure 32a). In order to prepare ANAUs with smaller gaps, UCs were drop-casted on the poly(methyl methacrylate) (PMMA) layer-coated substrate. After drop-casting of UCs, the sample was oxygen plasma treated to elevate UCs from the substrate to prevent connection between the Au layer on UCs and the Au layer on the substrate for high-angle deposition of the Au layer. Then, the Au layer (30 nm) was deposited onto UCs by physical vapor deposition, tilted at certain angles (0, 20, 40, and 60°) to assemble the nanocrescent antenna on the UCs. ANAUs were released from the substrate by sonication, then drop-casted on the TEM grid (Figures 32b). According to TEM imaging, the ANAU consists of a plasmonic antenna in a nanocrescent shape on the spherical dielectric core (UC; diameter: 70.4 nm) in a sub-wavelength size (λ_{ex}: 980nm). Correlated dark-field scattering images and upconversion luminescence images of ANAUs are depicted in Figures 32c and d. In order to obtain the correlated dark-field scattering and upconversion luminescence images, the substrate is located between the objective lens and the dark-field condenser. Since metallic nanoparticles have a characteristic color in scattered images regarding the onset of localized surface plasmon resonance (LSPR), ANAUs are seen as orange dots in dark-field scattering images. In upconversion luminescence images, ANAUs are seen as blue dots, and these two images are overlapping. Then, we obtained the dark-field scattering spectrum from individual ANAUs (Number 1, blue dot) and UCs (Number 2, gray dot), which is related to the characteristic LSPR of the nanocrescent antenna (Figure 32f). The spectral position of LSPR of ANAU obtained from the dark-field scattering measurement (blue dot) is around 597 nm and well matched with the simulation result of scattering cross-section calculation (blue line). The position of LSPR can be modulated by controlling the size of the nanocrescent antenna by using UCs with different sizes. The spectrum of upconversion luminescence of individual ANAUs (red line) and ensemble averaged ANAU clusters (blue line) are depicted in Figure 32g. To obtain the upconversion luminescence spectrum of individual ANAUs, excitation light (cw laser, $\lambda = 980$ nm) is focused on individually separated ANAUs using a 100x/1.3 NA objective lens. Then zeroth order diffraction image of individual ANAUs is obtained by spatially confining the region of interest (ROI) using a slit. To measure the ensemble averaged spectrum, excitation light is focused on the ANAU powder using a 10x/0.25 NA objective lens. Under 980 nm laser excitation, Tm^{3+} ions are excited by energy transfer through $Yb^{3+} \rightarrow Tm^{3+}$ and UC exhibited peaks at 450nm ($^1D_2 \rightarrow {}^3F_4$) and 474 nm ($^1G_4 \rightarrow {}^3H_6$) corresponding to the relaxation of electrons in the Tm^{3+}. The emission spectrum of the individual ANAU (redline) and ensemble averaged ANAU powder (redline) showed a high resemblance, but the full width at half maximum (FWHM) of the peaks in the ensemble averaged ANAU is wider. Since both spectra were obtained with the same detection system, this difference could not be originated to instrumental artifacts. This discrepancy is originated by the UC-UC interaction process, which is related to nonradiative and radiative energy transfer among adjacent Tm^{3+} ions. Figure 32h shows the representative upconversion luminescence spectrum of single ANAU (Number 1, blue line) and UC (Number 2, gray dotted line). Upconversion luminescence of UC is enhanced by 16.1 times after assembled with the Au nanocrescent antenna.

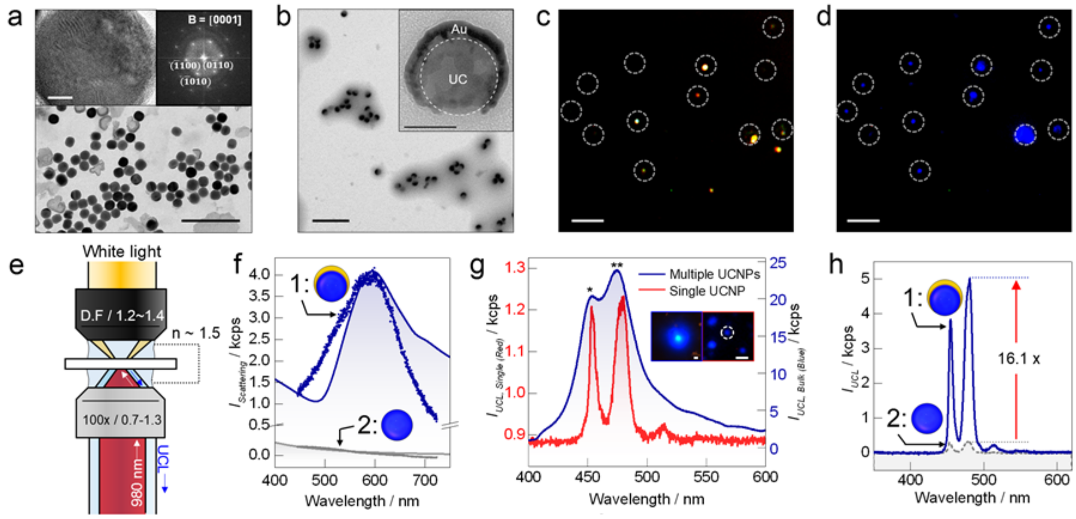

Figure 32. Optimization of nanofocusing of excitation light. (a) Transmission electron microscopy (TEM) image of upconversion nanoparticles (UCs; $NaYF_4$:Yb^{3+},Tm^3) (Scalebar:100nm). Inset is a high-resolution TEM image of a UC (Scalebar:10nm) with a selected area electron diffraction (SAED) pattern. (b) TEM image of ANAUs in low magnification (Scale bar: 1 µm) and high magnification (inset; scale bar: 50 nm). (c-d) Correlated image of (c) dark-field scattering and (d) frequency upconverted emission of ANAUs (Scale bar: 10 µm). (e) Schematic diagram for optical microscopy setup for correlated measurement of dark-field scattering and frequency upconverted emission. (f) Simulated scattering cross-section (line) and dark-field scattered spectrum of an ANAU (number 1, blue) and UC (number 2, gray). (g) Frequency upconverted emission spectrum of single ANAU (red) and ensemble averaged ANAU powder (blue). The inset shows CCD images obtained from each sample (Scale bar at left: 10 µm, right: 1 µm). (h) Representative frequency upconverted emission spectrum of an ANAU (number 1) and UC (number 2).

III-D-3. Determination of nanomolar levels of reactive oxygen species in microorganisms and aquatic environments using a single nanoparticle-based optical sensor (Korea team)

Reactive oxygen species (ROS) are strong oxidants, and have attracted considerable attention in both biological and environmental fields. Although various methods for ROS detection, including optical and electrochemical techniques, have been developed, they still face challenging issues in terms of poor sensitivity, reproducibility, stability, and in vivo applicability. In this project, we present sensitive and selective optical sensor for ROS detection, based on single plasmonic nanoprobes and redox-active cytochrome c (Cyt c)-mediated plasmon resonance energy transfer. By measuring the spectral changes of plasmonic nanoprobes, derived from the unique molecular absorption of Cyt c, we sensitively monitored ROS generated in *Caenorhabditis elegans* (*C. elegans*) exposed to graphene oxide.

ROS detection method using a single nanoparticle-based optical sensor: The ROS detection strategy for nanotoxicity evaluation and environmental monitoring is shown in Figure 33. A small aliquot (usually < 20 mL) of sample solution is placed on a nanoparticle-immobilized sensor chip, which is promptly monitored by dark-field microscopy combined with a spectrophotometer (Figure 33a). Our sensing protocol is based on the PRET phenomena between the single nanoparticle probe and redox active Cyt c, since Cyt c absorbs Rayleigh scattering from the nanoparticle when it is placed in proximity to it (Figs. 33b). Figure 33c-h clearly shows quenching dips matching with absorption peaks of Cyt c. The sensing principle is a vertical quenching dip correlated with absorption peaks of Cyt c according to the change in redox state. Prior to detecting ROS generated in real biological and environmental samples, we first acquired calibration curves using our newly developed single nanoparticle-based detection method.

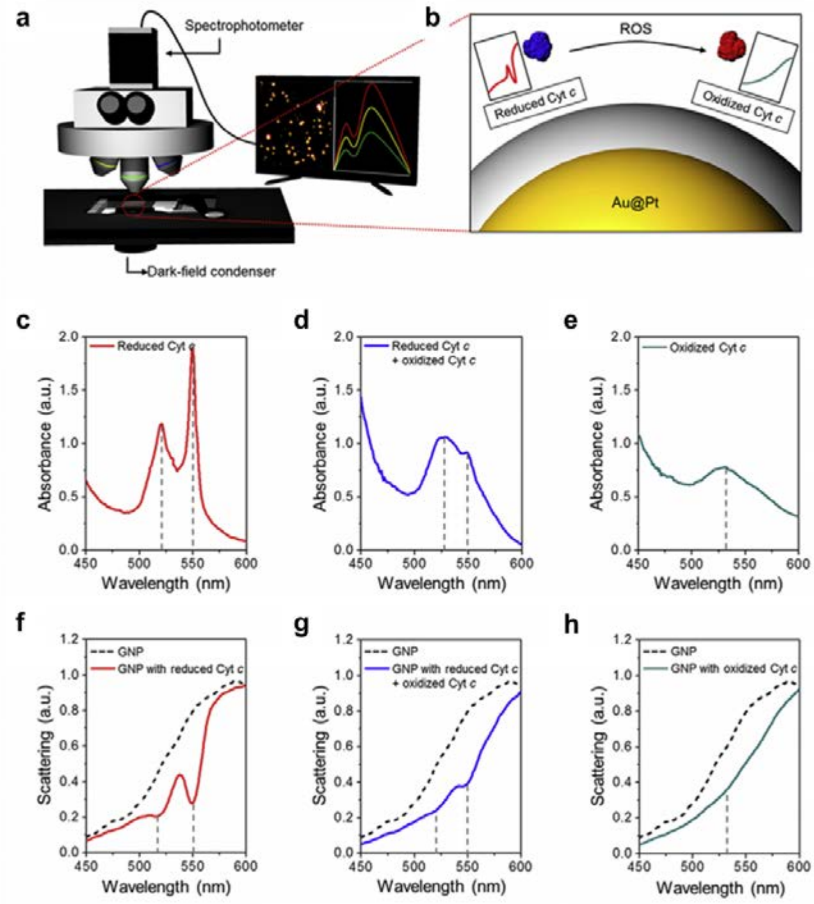

Figure 33. Description of a ROS detection method using a single nanoparticle-based optical sensor. (a) Configuration of the optical monitoring system based on a dark-field microscopy combined with a spectrophotometer. (b) Illustration showing dynamic spectral change in quenching dip in accordance with redox state of Cyt c induced by ROS. (c-e) Intrinsic absorption peaks of fully reduced Cyt c (c), mixture of reduced Cyt c and oxidized Cyt c (d), and fully oxidized Cyt c (e). (f-h) Rayleigh scattering spectra of gold nanoparticle with fully reduced Cyt c (f), mixture of reduced Cyt c and oxidized Cyt c (g), and fully oxidized Cyt c (h).

Detection of ROS generation in C. elegans during exposure to GO for nanotoxicity evaluation: *C. elegans* is one of the most extensively used model organisms for biological and environmental studies. Owing to its transparency, which permits particular strength for studying uptake and distribution of nanoparticles and also to its genetic power for mechanism study, it has been frequently utilized to evaluate nanotoxicity. To monitor ROS generation in *C. elegans*, we incubated them with graphene oxide (GO), which has been reported as a toxic nanomaterial (Figure 34a). Raman spectra (Figure 34b) collected inside *C. elegans* show characteristic peaks at 1348 cm^{-1} (D-band) and 1607 cm^{-1} (G-band) for the internalized GO. To further investigate the distribution of GO in *C. elegans*, Raman mapping was also carried out with the G-band of GO and the result clearly showed a noticeable presence in the internal organs (especially intestine) of *C. elegans* (Figure 34c).

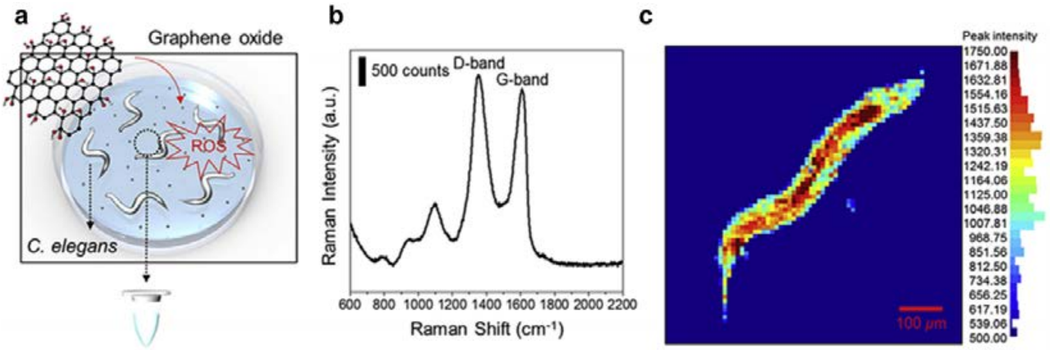

Figure 34. Detection of ROS generation in *C. elegans* during exposure to GO for nanotoxicity evaluation. (a) A graphic illustration of sampling procedures for the detection of ROS generated by *C. elegans*. (b) A characteristic Raman spectrum of GO internalized in *C. elegans*. (c) A Raman mapping image of the distribution of GO (100 mg L^{-1}) in *C. elegans*.

III-D-4. Development of technique for the ultra-sensitive identification of waterborne pathogens via liquid/liquid interface SERS (Korea Team)

After self-assembling metallic nanoparticles on the surface of pathogens, and successively mixing the solution with oleic acid, nanoparticle-assembled pathogens were successfully enriched at the liquid/liquid interface (Figure 35). Figure 36a shows real images of process of bacterial enrichment at liquid/liquid interface. The experimental results show that the required time for enrichment at interface of bacteria with the rod-shaped 2-dimensional metallic nanoparticle (i.e., GNR) is less than 3 minutes. As shown in figure 36b, by illuminating laser to the interface with enriched nanoparticle-assembled pathogens, Raman signal of waterborne pathogen was successfully obtained via interfacial surface-enhanced Raman spectroscopy. Raman transitions of enriched bacteria at liquid/liquid interface can be assigned as Raman signal from bacteria were observed. The specific Raman transitions, 765 cm^{-1} can be assigned to O-specific polysaccharide.

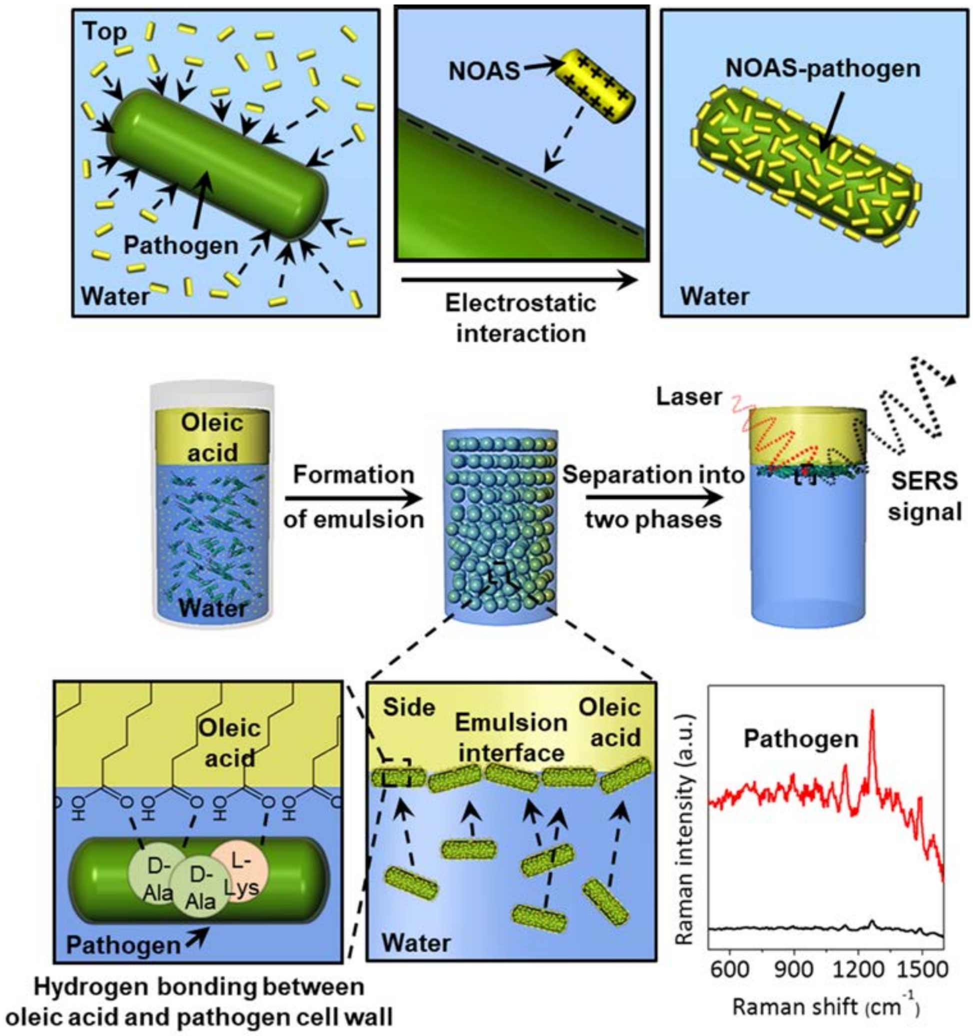

Figure 35. Schematic illustration of liquid/liquid interface SERS for waterborne pathogen detection. Metallic nanoparticles are self-assembled on the surface of waterborne pathogens. Plasmonic bacteria which was densely covered with metallic nanoparticle were formed emulsion via simple mixing with oleic acid. A carboxylic acid of oleic acid interacts with specific amino acid (*i.e.*, Ala, Lys) on the surface of bacteria through hydrogen boding enriching the bacteria at liquid/liquid interface.

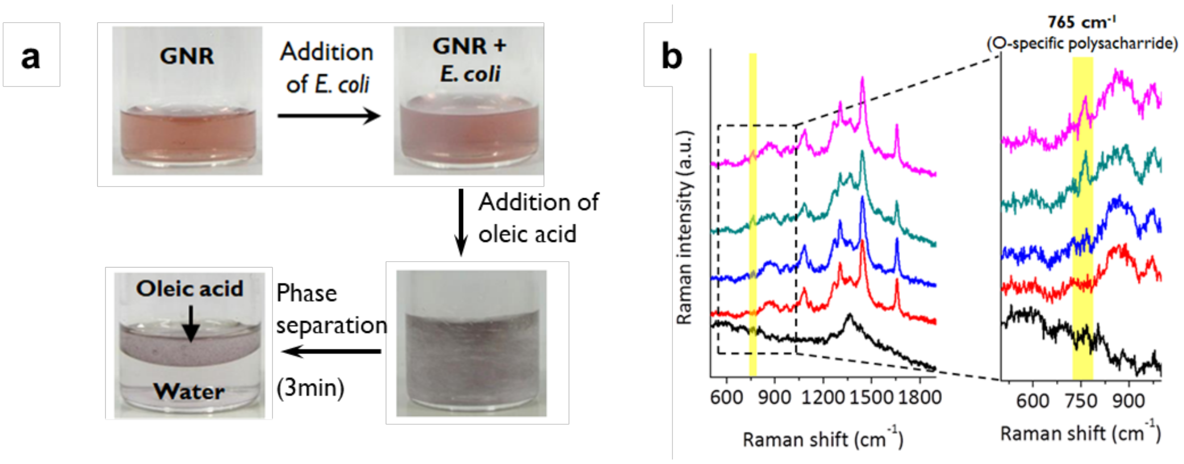

Figure 36. The experimental process of bacteria enrichment at liquid/liquid interface and Raman measurement results of GNR-assembled bacteria at liquid/liquid interface

III-D-5. Assessing antibiotic permeability of gram-negative bacteria via nanofluidics (U.S. team)

Drug discovery has proven to be extremely difficult while antibiotic resistance has increased rapidly. Due to antibiotic resistance some bacterial infections turn into a deadly health condition. An important challenge in antibiotic discovery is to devise powerful molecules that enter gram-negative bacteria and avoid active spillage. An important analysis of rational drug design is challenging because of the lack of effective analytical tools for analyzing the bacterial membrane permeability of small molecules. We design, manufacture, and characterize nanofluidic devices that actively load more than 200 single bacterial cells in a nanochannel array. We show a gigaohm seal between the nanochannel wall and the loaded bacteria, limiting the small molecule migration that occurs only through the bacterial cell envelope. The quantification of clindamycin translocation through wild-type and efflux-deficient (Δ *tol*C) Escherichia coli strains via nanofluid-interface liquid chromatography mass spectrometry reveals a higher level of translocation to wild-type Escherichia coli compared to flow-through deficiency strains. We believe that the evaluation of compound permeability of Gram negative bacteria through a nanofluidic analysis platform will be an important tool for studying bacterial infiltration and outflow of bacteria to help design rational antibiotics.

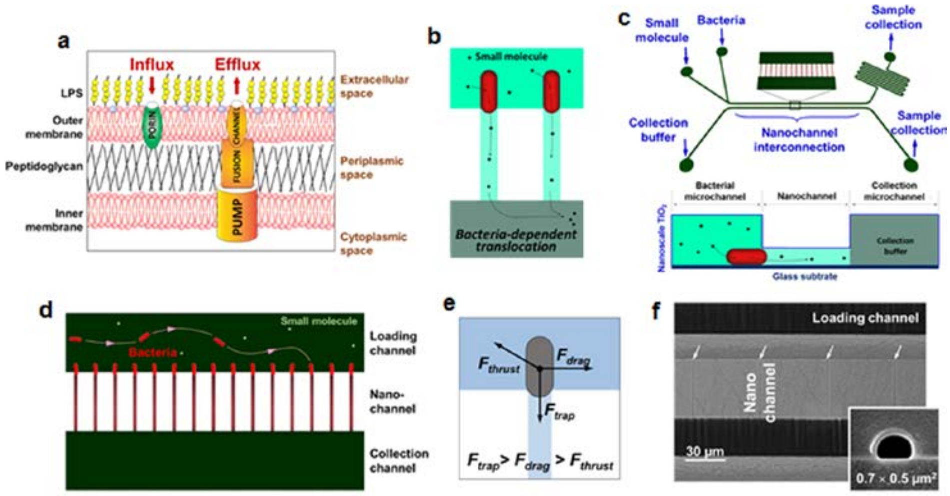

Figure 37. Analytic nanofluidics for direct quantitation of molecular translocation across the bacterial cell envelope. (a) Illustration of the Gram-negative bacterial cell envelope. Porins and efflux pump systems are also shown in the illustration, which are mechanisms for influx and efflux, respectively, and are thought to be the main entry and exit points for antibiotics. (b) Concept of analytic nanofluidics to evaluate bacterial pharmacokinetics. The red rod shapes represent bacterial cells, and the other colored sections indicate different fluidic compartments. (c) Schematics of the fluidics device showing two parallel microchannels interconnected with an array of nanochannels. As shown in the cross-sectional view, the chemical barrier integrated on the device surfaces prevented the loss of small molecules and enabled precise quantitation of molecular translocation (c, bottom). (d) Active flow in the cell-loading channel delivers bacteria to the nanochannel array. (e) A cross section of the nanochannels is shown in the inset. (f) SEM images of the device showing the microchannels connected by the nanochannel array.

IV. Achievement and Contribution on Related Field

IV-1. Publications and Discoveries

Title	Authors	Journal/Volume/Year	DOI
Immiscible Oil-Water Interface: Dual Function of Electrokinetic Concentration of Charged Molecules and Optical Detection with Interfacially-trapped Gold Nanorods	Hye Soo Han, Jihwan Song, Joohee Hong, Dongchoul Kim and Taewook Kang	*Analytical Chemistry*/**86**/2014	10.1021/ac501378x
Two-dimensional Hyper-branched Gold Nanoparticles Synthesized on a Two-dimensional Oil/Water Interface	Yonghee Shin, Chiwon Lee, Myungseok Yang, Sunil Jeong, Dongchoul Kim and Taewook Kang	*Scientific Reports*/ **4**/2014	10.1038/srep06119
Label-free Density Difference Amplification-based Cell Sorting	Jihwan Song, Minsun Song, Taewook Kang, Dongchoul Kim and Luke P. Lee	*Biomicrofluidics*/**8**/ 2014	10.1063/1.4902906
Equilibrium Morphology of Plasmonic Au/Polystyrene Dimeric Nanoparticle	Myungseok Yang, Sunil Jeong, Taewook Kang and Dongchoul Kim	*Journal of Physical Chemistry C*/**119**/ 2015	10.1021/jp509508s
Interfacial Synthesis of Two-Dimensional Dendritic Platinum Nanoparticles Using Oleic Acid-in-Water Emulsion	Eui-Geun Jung, Yonghee Shin, Minzae Lee, Jongheop Yi and Taewook Kang	*ACS Applied Materials & Interfaces*/**7**/2015	10.1021/acsami.5b02433
Facile Preparation of Ultrasmall Void Metallic Nanogap from Self-Assembled Gold-Silica Core-Shell Nanoparticles Monolayer via Kinetic Control	Yuna Shin, Jihwan Song, Dongchoul Kim and Taewook Kang	*Advanced Materials*/**27**/2015	10.1002/adma.201501163
Bioinspired optical antennas: gold plant viruses	SoonGweon Hong, Mi Yeon Lee, Andrew O Jackson and Luke P. Lee	*Light:Science & Applications*/**4**/ 2015	10.1038/lsa.2015.40
Rapid Optical Cavity PCR	Jun Ho Son , SoonGweon Hong , Amanda J. Haack, Lars Gustafson , Minsun Song ,Ori Hoxha and Luke P. Lee	*Advanced Healthcare Materials*/**5**/2016	10.1002/adhm.201500708
Spontaneous Self-Formation of 3D Plasmonic Optical Structures	Inhee Choi, Yonghee Shin, Jihwan Song, Soongweon Hong, Younggeun Park, Dongchoul Kim, Taewook Kang and Luke P. Lee	*ACS Nano*/**10**/ 2016	10.1021/acsnano.6b02903
General and Programmable Synthesis of Hybrid Liposome/metal Nanoparticles	Jin-Ho Lee, Yonghee Shin, Wooju Lee, Dongchoul Kim, Luke P. Lee, Jeong-Woo Choi and Taewook Kang	*Science advances*/**2**/2016	10.1126/sciadv.1601838

Assessing Antibiotic Permeability of Gram-Negative Bacteria via Nanofluidics	SoonGweon Hong, Tobias J. Moritz, Christopher M. Rath, Pramila Tamrakar, Philip Lee, Thomas Krucker and Luke P. Lee	*ACS Nano*/**11**/2017	10.1021/acsnano.7b02267
Asymmetric Nanocrescent Antenna on Upconversion Nanocrystal	Doyeon Bang, Eun-Jung Jo, SoonGweon Hong, Ju-Young Byun, Jae Young Lee, Min-Gon Kim and Luke P. Lee	*Nano Letters*/**17**/2017	10.1021/acs.nanolett.7b02327
Determination of nanomolar levels of reactive oxygen species in microorganisms and aquatic environments using a single nanoparticle-based optical sensor	Yura Kim, Youngho Kim, Jinhee Choi, Taewook Kang and Inhee Choi	*Analytica Chimica Acta*/**967**/2017	10.1016/j.aca.2017.03.012
Plasmonic Bacteria-on-Nanoporous Mirror via Hydrodynamic Trapping for Rapid Identification of Waterborne Pathogens	Keumrai Whang, Jong-Hwan Lee, Yonghee Shin, Wooju Lee, Young Wan Kim, Dongchoul Kim, Luke P. Lee and Taewook Kang	*ACS Nano* (under review)	

IV-2. Patents

Patents: METHOD FOR PREPARING A DENDRIMER TYPE OR DENDRIMER-DERIVED METAL NANOSTRUCTURE IN LIQUID-LIQUID INTERFACE AND DENDRIMER TYPE OR DENDRIMER-DERIVED METAL NANOSTRUCTURE PREPARED BY SAME, PCT/KR2013/010568

IV-3 Team Collaboration Synergy Highlights

- 4 visiting post-doc for 4 years
- 4 visiting graduate students for 4 years
- PIs of both groups frequently made a regular-based actual site visits to exchange ideas and share progresses
- Exchange of as-prepared unconventional metal nanoparticles and data for optimization of the nanoparticles (more than 4 times per year)
- 4 joint papers in high-impact journals (3 papers – published/ 1 paper – under review)

IV-4. Expected Contribution

The expected contribution of the results from this research is as below.

1) Development of new methodologies for synthesizing, optimizing and utilizing the unconventional metallic nanostructures based on interfacial nanosystems
   - For the rational synthesis of unconventional metallic nanoparticles

- For the controlled assembly of unconventional metallic nanoparticles
- For molecular imaging and sensing probes

2) Development of ultra-fast molecular detection systems with high accuracy, sensitivity, and selectivity by utilizing newly created metallic nanostructures
   - For environmental pollutant monitoring
   - For food safety monitoring
   - For monitoring pathogenic bacteria detection including airborne diseases
3) Development of integrated molecular diagnostic platforms by utilizing newly created 3D plasmonic structures with integrated metallic nanoparticles
   - For quantitative and qualitative detection of biomarkers for diseases
   - For point-of-care biosensors and portable sensing platforms
   - For high spatial molecular imaging and molecular delivery
4) Creation of new and high-value-added research fields derived from systematic approaches including theoretical simulation and experimental demonstration
   - For studying interactions at interfaces in vivo (e.g., membrane transport, molecular signaling pathway, cellular metabolism and so on.)
   - For understanding characteristic interactions of nanostructures via studying heat transfer and chemical reactions at nanoscale.
5) Achievement of generic technology and promotion of licensing transfer for commercialization through patent applications and registrations

V. References

[1] Chia-Yang Tsai, Jyun-Wei Lin, Che-Yao Wu, Pin-Tso Lin, Tsan-Wen Lu, and Po-Tsung Lee, *Nano letters* **2012**, 12, 1648-1654

[2] Xiaohu Xia and Younan Xia, *Nano letters* **2012**, 12, 6038-6042

[3] Mehmet Yilmaz, Erhan Senlik, Erhan Biskin, Mustafa Selman Yavuz, Ugur Tamere and Gokhan Demirel, *Physical Chemistry Chemical Physics* **2014**, 16, 5563-5570

[4] Edgar González, Jordi Arbiol, and Víctor F. Puntes, *Science* **2011**, 334, 1377-1380

[5] Alastair W. Wark, Robert J. Stokes, Steven B. Darby, W. Ewen Smith, and Duncan Graham, *Journal of Physical Chemistry C* **2010**, 114, 18115-18120

[6] F. De Angelis, F. Gentile, F. Mecarini, G. Das, M. Moretti, P. Candeloro, M. L. Coluccio,

G. Cojoc, A. Accardo, C. Liberale, R. P. Zaccaria, G. Perozziello, L. Tirinato, A. Toma, G. Cuda, R. Cingolani, and E. Di Fabrizio, *Nature Photonics* **2011**, 5, 682-687

[7] Chenxu Yu and Joseph Irudayaraj, *Analytical Chemistry* **2007**, 79, 572-579

[8] Zhiqin Yuan, Fengniu Lu, Meihua Peng, Chia-Wei Wang, Yu-Ting Tseng, Yi Du, Na Cai, Chia-Wen Lien, Huan-Tsung Chang, Yan He, and Edward S. Yeung, *Analytical Chemistry* **2015**, 87, 7267-7273

[9] Hyungwon Moon, Dinesh Kumar, Haemin Kim, Changbeom Sim, Jin-Ho Chang, Jung-Mu Kim, Hyuncheol Kim, and Dong-Kwon Lim, *ACS Nano* **2015**, 9, 2711-2719

[10] Aravind Kumar Rengan, Amirali B. Bukhari, Arpan Pradhan, Renu Malhotra, Rinti Banerjee, Rohit Srivastava, and Abhijit De, *Nano Letters* **2015**, 15, 842-848

[11] Chunyu Niu, Bingfang Zou, Yongqiang Wang, Lin Cheng, Haihong Zheng, and Shaomin Zhou, *Langmuir* **2016**, 32, 858-863

[12] Kun Zhang, Jingjing Zhao, Huiying Xu, Yixin Li, Ji Ji, and Baohong Liu, *ACS Applied Materials & Interfaces* **2015**, 7, 16767-16774

[13] Premasiri, W. R., et al. "Characterization of the surface enhanced Raman scattering (SERS) of bacteria." *The journal of physical chemistry B* **2005**, 109, 312-320.

[14] Yang, Danting, et al. "Reproducible E. coli detection based on label-free SERS and mapping." *Talanta* **2016**, 146, 457-463.

[15] Zhou, Haibo, et al. "SERS detection of bacteria in water by in situ coating with Ag nanoparticles." *Analytical chemistry* **2014**, 86, 1525-1533.

[16] Lin, Hsing-Ying, et al. "On-line SERS Detection of Single Bacterium Using Novel SERS Nanoprobes and A Microfluidic Dielectrophoresis Device." *Small* **2014**, 10, 4700-4710.

[17] Harms, Gerda, et al. "Real-time PCR quantification of nitrifying bacteria in a municipal wastewater treatment plant." *Environmental science & technology* **2003**, 37, 343-351.

[18] Czilwik, G., et al. "Rapid and fully automated bacterial pathogen detection on a centrifugal-microfluidic LabDisk using highly sensitive nested PCR with integrated sample preparation." *Lab on a Chip* **2015**, 15, 3749-3759.

[19] Safavieh, Mohammadali, et al. "A simple cassette as point-of-care diagnostic device for naked-eye colorimetric bacteria detection." *Analyst* **2014**, 139, 482-487.

[20] Kersting, Sebastian, et al. "Multiplex isothermal solid-phase recombinase polymerase amplification for the specific and fast DNA-based detection of three bacterial pathogens." *Microchimica Acta* **2014**, 181 1715-1723.